# The relationship between gold mineralization, exhumation of metamorphic core complex and magma cooling: Formation of the Anjiayingzi Au deposit, northern North China Craton

Lebing Fu [a,*], Junhao Wei [a], Huayong Chen [b], Leon Bagas [c], Jun Tan [a], Huan Li [a], Daohan Zhang [a], Ning Tian [a]

[a] Faculty of Earth Resources, China University of Geosciences, Wuhan 430074, China
[b] Key Laboratory of Mineralogy and Metallogeny, Guangzhou Institute of Geochemistry, Chinese Academy of Sciences, Guangzhou 510640, China
[c] Centre for Exploration Targeting, ARC Centre of Excellence for Core to Crust Fluid Systems, University of Western Australia, 35 Stirling Highway, Crawley, WA 6009, Australia

## ARTICLE INFO

## ABSTRACT

The Anjiayingzi gold deposit is hosted by the Jiguanzi Quartz Monzonite in the footwall of the Kalaqin Metamorphic Core Complex (MCC) at Chifeng in the northern part of the North China Craton (NCC). An earlier (ca. 135–125 Ma) top-to-the-NE ductile–brittle shear and a later (ca. 121 Ma) top-to-the-NW and SE brittle detachment normal faulting are recognized around the Kalaqin MCC. The Jiguanzi Quartz Monzonite intruded the footwall of the Kalaqin MCC at ca. 133 ± 1 Ma with crystallization temperatures of 640–691 °C, pressures of 167–271 MPa and an average depth of 8.6 km. Gold veins in the Anjiayingzi gold deposit are hosted by the monzonite and controlled by the NE-trending brittle–ductile and brittle fault zones. These ore-bearing faults are products of a regional sinistral shearing event coinciding with the earlier top-to-the-NE ductile–brittle shear at the Kalaqin MCC. The ore of the Anjiayingzi deposit is characterised by its low Au/Ag ratio (<1) and high sulphide content (4–30 vol.%). The assemblage associated with gold mineralization consists of: (1) quartz–coarse-grained pyrite; (2) quartz–fine-grained pyrite; (3) quartz–polymetallic sulphide; and (4) quartz–carbonate. The ore formed at 245–358 °C from a $H_2O$–$CO_2$–NaCl fluid system with salinities of 1.3–15.6 wt.% NaCl equiv. Trapping pressures of ore fluids were 50–110 MPa, corresponding to an average depth of ~2.5 km under a lithostatic load and ~7.5 km under a hydrostatic load. Fluid mixing and immiscibility are potential causes for the rapid precipitation of sulphides carrying Au. The stable isotope $\delta D$ (−80.3 to −96.5‰) and $\delta^{18}O_{H_2O}$ (3.7 to 5.5‰) of the ore fluids, the consistent Pb isotope compositions between the ore-bearing sulphides and K-feldspar from the Jiguanzi Quartz Monzonite, and a >2 billion year time gap between the gold mineralization and metamorphism of the basement all indicate that the mineralizing fluids and metals are derived from a concealed intrusion near the major eastern Louzidian Fault in the Kalaqin MCC. This proposal is supported by the presence of mafic magmatic enclaves and rhyolite dykes in the Jiguanzi Quartz Monzonite, and higher average $Th_{total}$ (322 °C) and $\delta^{34}S$ (2.4‰) of Eastern veins than those of Western veins (with a $Th_{total}$ of 287 °C and $\delta^{34}S$ value of 0.3‰). The ca. 133–126 Ma gold mineralization at Anjiayingzi was formed during rapid cooling of ca. 133–126 Ma Jiguanzi Quartz Monzonite at a cooling rate of 42–71 °C/Ma, and fast exhumation and cooling of the Kalaqin MCC between ca. 135 and 121 Ma at a cooling rate of 30 °C/Ma. This process was accompanied by fluid immiscibility and mixing within the structural transition from ductile–brittle to brittle deformation with resultant fluid-pressure fluctuations between the supra-hydrostatic and hydrostatic regimes.

## 1. Introduction

Numerous vein-gold deposits are located along the margins of the North China Craton (NCC), which have been historical sources for gold (Fig. 1a; Goldfarb and Santosh, 2014; Li et al., 2012a; Yang et al., 2003). Many of these deposits have a close spatial association with metamorphic core complexes (MCCs), uplifted Precambrian rocks, and crustal–mantle derived granites (Figs. 1 and 2; Charles et al., 2013; Fu et al., 2012b; Goldfarb and Santosh, 2014; Li et al., 2012a; Yang et al., 2003). Large examples of gold deposits in the northern NCC are the Anjiayingzi, Jinchanggouliang, and Paishanlou gold deposits from the Chifeng–Chaoyang gold field (Figs. 1a–b and 2). Anjiayingzi is located near the Jiguanzi Quartz Monzonite in the Kalaqin MCC, Jinchanggouliang is located near the Duimiangou Intrusion in the Nulu'erhu Uplift, and Paishanlou is near the Dashitougou Intrusion in the Yiwulüshan MCC (Fig. 1b; Fu et al., 2012b; Miao et al., 2003; Sun et al., 2012; Zhang et al., 2005). Other deposits include Wulong close to the Sanguliu Granite in the Liaonan MCC of northeastern

* Corresponding author at: Faculty of Earth Resources, China University of Geosciences, Lumo Road No. 388, Hongshan District, Wuhan 430074, Hubei Province, China. Tel.: +86 13429802569; fax: +86 27 67883053.
E-mail addresses: fulebing1212@126.com, fulebing1212@gmail.com (L. Fu).

NCC (Liu et al., 2013; Wei et al., 2002), and the well-known Jiaojia and Linglong gold deposits in the Jiaodong gold field located near the Guojialing Granite in the Linglong MCC (Charles et al., 2011, 2013). Similarly, more than 40 gold deposits in the Xiaoqinling gold field of southern NCC are located in and around the Huashan, Wenyu and Niangniangshan granites in the Xiaoqinling MCC (Li et al., 2012a; Zhao et al., 2012; Zhou et al., 2014).

Temporally, the Early Cretaceous (ca. 130 and 110 Ma) large-scale gold deposits appear to be contemporaneous with the formation of the MCCs (e.g., Wang et al., 2011; Zhu et al., 2012), magmatism (e.g., Wu et al., 2005), and formation of the extensional basins (Fig. 1a–b; Meng, 2003; Zhu et al., 2012). They are interpreted to result from lithospheric thinning and destruction of the NCC in an extensional regime (Goldfarb and Santosh, 2014; Li and Santosh, 2014; Li et al., 2012a; Mao et al., 2008; Yang et al., 2003; Zhai and Santosh, 2013).

Typical MCCs from the NCC have three essential components. These are: (1) a master shallow- to moderate-dipping detachment fault; (2) a footwall consisting of fault-related mylonitic rocks, and (3) a hanging wall of upper crustal basement rocks (Davis and Zheng, 2002; Whitney et al., 2013). The master detachment fault generally extends

to mid-crustal depths or below the brittle–ductile transition zone at a depth of ~10–15 km where quartz becomes plastic (Davis and Zheng, 2002). Mylonitic rocks in the footwall are often formed at greenschist–amphibolite facies conditions at temperatures of ~400–550 °C (Davis and Zheng, 2002; Yao et al., 2007). The initiation and exhumation of MCC started with hot ductile deformation, which gradually changed to cool brittle deformation accompanied by transfer of heat and material from deeper to shallow levels (Whitney et al., 2013). Interestingly, most gold deposits from the NCC are also in association with brittle to brittle–ductile faults (Goldfarb and Santosh, 2014; Hart et al., 2002; Li et al., 2012a), which are located near or within MCCs. Based on the close spatial relationships and the similar structural regimes described above, the large-scale gold mineralization and MCC development may be genetically associated, and they are probably both related to regional magmatism.

The relationship between MCC exhumation, magma cooling and gold mineralization from the NCC has not been adequately described, though there are some references touching on this issue (Charles et al., 2011; Yang et al., 2014). The contemporaneous occurrences of
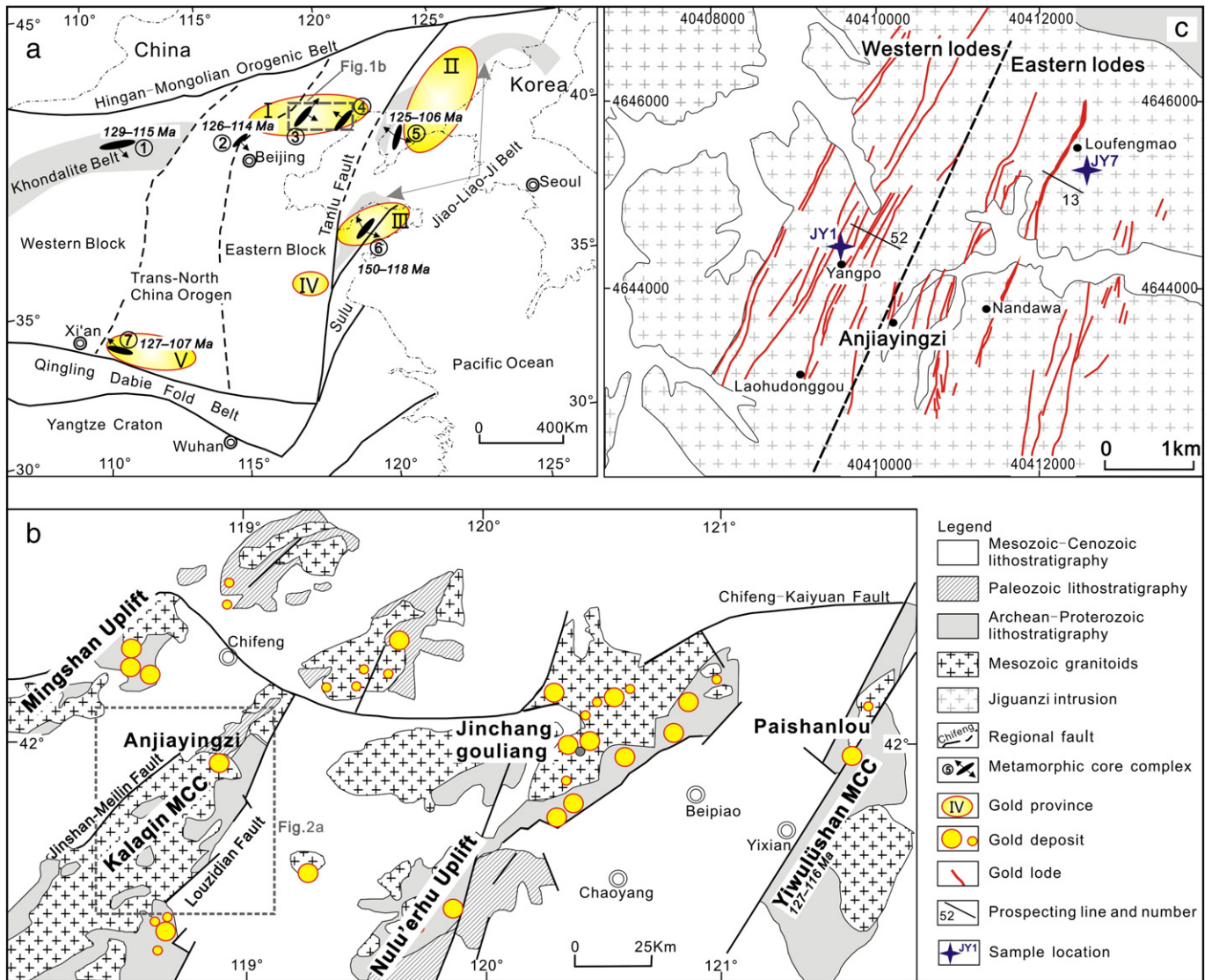


**Fig. 1.** Simplified geology of: (a) the eastern China with the Western Block, Trans-North China Orogen and Eastern Block of the NCC (Fu et al., 2012b; Zhao and Zhai, 2013); (b) the Chifeng–Chaoyang gold field showing the distribution of the Early Cretaceous MCCs, Mesozoic granites, and gold deposits (Fu et al., 2012b; Yang et al., 2003); and (c) the Anjiayingzi gold deposit showing sample locations of the Jiguanzi Quartz Monzonite. The ellipses with arrows (1–7) and ages in (a) represent locations, extension directions and formation ages of the Daqingshan, Yunmengshan, Kalaqin, Yiwulüshan, Liaonan, Linglong and Xiaoqinling MCCs, respectively (Charles et al., 2013; Lin et al., 2013b; Yang et al., 2007). Gold fields: I — Zhangjiakou–Chifeng–Chaoyang, II — Liaodong, III — Jiaodong, IV — Luxi, V — Xiaoqinling–Xiongershan.

the Anjiayingzi gold deposit, Jiguanzi Quartz Monzonite and Kalaqin MCC provide a case for investigation. In this contribution, we present new zircon U–Pb dates for the monzonite, and temperature–pressure–depth estimates for both the intrusion and associated Anjiayingzi gold deposit from the Kalaqin MCC. In combination with the geology of the deposit, ore fluid geochemistry, and previous geological and thermochronometric data for the Kalaqin MCC, this information is used to help decipher the relationships between gold mineralization, magmatism and MCC development, and further provide constraints on the mineralization process responsible for vein gold deposition in the region.

## 2. Geological setting

### 2.1. Geology of the NCC

Precambrian units are extensive in the NCC and make up the granulite to amphibolite facies mafic to felsic volcanic and sedimentary rocks that up to ca. 3.8 Ga (Jahn et al., 1987; Wu et al., 2008). The Hingan–Mongolian or Central Asia Orogen binds the NCC to the north, the Qinling–Dabie–Sulu Fold Belt to the south, and the Mesozoic Paleo-Pacific/Izanagi plate to the east and southeast (Fig. 1a; Maruyama et al., 1997; Zhu et al., 2012).

The NCC is subdivided into the Eastern Block, Trans-North China Orogen and Western Block (Fig. 1a; Zhao et al., 2001). The Neoarchean units in the Eastern and Western blocks include 2.8–2.7 Ga and 2.6–2.5 Ga tonalitic–trondhjemitic–granodioritic (TTG) gneisses and mafic to komatiitic rocks (Zhai and Santosh, 2011; Zhao and Zhai, 2013). The intervening Trans-North China Orogen is a collisional belt along which the Eastern and Western blocks were assembled to form the NCC during the Paleoproterozoic (Zhao and Zhai, 2013). Two Paleoproterozoic assemblages recently recognized are the Khondalite Belt in the Western Block and the Jiao–Liao–Ji Belt in the Eastern Block (Fig. 1a; Zhai and Santosh, 2011; Zhao and Zhai, 2013). Although models for the final assemblage of Precambrian terranes to form the NCC are still controversial, most researchers propose that the "cratonization" ended after the major Paleoproterozoic orogenies across the NCC, as evidenced by the subsequent 1.80–1.78 Ga mafic dyke swarms and the Late Paleoproterozoic to Neoproterozoic multiple rift basins (Zhai and Santosh, 2011).

The NCC was reactivated during the Paleozoic–Mesozoic along the northern and southeastern margins. The Central Asia Orogen collided with the craton to the north during the Middle Triassic resulting in the closure of the Paleo-Asian Ocean (Fig. 1a; Chen et al., 2009; Fu et al., 2012a; Xiao et al., 2009; Zhang et al., 2009). The Qinling–Dabie–Sulu Fold Belt to the south also developed during the Triassic in response to the collision of Yangtze Craton with the NCC (Zheng et al., 2012). During this period, the NCC was subjected to intense compressional deformation that relaxed and led to extensional deformation during the late Jurassic to early Cretaceous (Davis et al., 1998; Kusky et al., 2007; Lin et al., 2013a). As a result of this change in deformation regime, the extensional deformation rotated clockwise from WNW–ESE in the Early Cretaceous to NW–SE in the latest Early Cretaceous (Zhu et al., 2012). The clockwise change in the extension direction is consistent with the shift in the movement direction of the subducted Paleo-Pacific/Izanagi block (Sun et al., 2007; Tan et al., 2007; Zhu et al., 2012).

### 2.2. Geology of the Chifeng–Chaoyang gold field

The Chifeng–Chaoyang gold field is located in the northern part of the NCC and comprises the NE-trending Mingshan and Nulu'erhu uplift belts and the Kalaqin and Yiwulüshan MCCs, which consist of Precambrian rocks intruded by Triassic to Cretaceous granites (Fig. 1a–b; Davis et al., 1998). The Precambrian rocks include the Neoarchean to Paleoproterozoic Jianping Group, which consist of ca. 2555–2550 Ma sedimentary and volcanic sequences, and ca. 2538–2495 Ma TTG

gneisses with different degrees of migmatization (Lin et al., 2013a; Liu et al., 2011). These successions were metamorphosed to granulite facies at ca. 2485 Ma and were retrogressed to greenschist facies between ca. 2450 and 2401 Ma (Liu et al., 2011). The Triassic magmatism is characterised by ca. 227 Ma shoshonitic dykes from the Nulu'erhu Uplift and may be the result of closure of the Paleo-Asian Ocean (Fu et al., 2012a). The Early Cretaceous intrusions are more widespread, such as the Jiguanzi Quartz Monzonite in the Kalaqin MCC (Fig. 2), the Duimiangou Intrusion in the Nulu'erhu Uplift (near the Jinchanggouliang deposit, Fig. 1b; Fu et al., 2012b; Miao et al., 2003), and the Dashitougou Intrusion in the Yiwulüshan MCC (near the Paishanlou deposit, Fig. 1b; Sun et al., 2012; Zhang et al., 2005).

About 50 gold deposits and prospects in the Chifeng–Chaoyang gold field are located either in Mesozoic granites or in the hornfels zones developed between the granites and the country rocks (Fig. 1b; Yang et al., 2003). Most of these deposits comprise auriferous quartz and sulphide-gold ores located in NE-trending faults. The Jinchanggouliang deposit in the Nulu'erhu Uplift has a molybdenite Re–Os age of 131 ± 1 Ma (Hou, 2011); and the Paishanlou deposit in the Yiwulüshan MCC has a biotite Ar–Ar age of ca. 127 Ma (Zhang et al., 2005). Thus, the timing of the gold in the Chifeng–Chaoyang field appears to be Early Cretaceous in age.

### 2.3. Geology of the Kalaqin MCC

The Kalaqin MCC extends northeast for a distance of 150 km and over a width of 40 km (Figs. 1b and 2a). The eastern Louzidian and western Jinshan–Meilin faults, interpreted as detachment faults, separate a crystalline footwall consisting of mylonitic gneiss and orthogneiss from the overlying non-mylonized gneiss and relatively non-deformed Early Cretaceous volcanic and sedimentary rocks, which were located in the eastern Pingzhuang and western Xiaoniu rift-basins (Fig. 2a; Han et al., 2001; Lin et al., 2013a). The core of the MCC consists of ca. 2555–2495 Ma metamorphosed sedimentary and volcanic rock sequences and TTG orthogneiss assigned to the Jianping Group. These rocks were metamorphosed between ca. 2485 and 2401 Ma (Liu et al., 2011), and are intruded by the Permian Guojiadian Granite, Triassic (ca. 231–204 Ma) Majiazi composite plutons, Jurassic (ca. 156 ± 2 Ma) Maanshan Granite, and Cretaceous (ca. 138–132 Ma) Jiguanzi Quartz Monzonite (Li et al., 2004b; Ouyang, 2010).

Previous studies of provenance and paleocurrent in the overlying rift-basins indicate that there were two periods of infill. The early input was from the southwest margin of the basins, and the later deposits were derived from the core of the MCC and transported outwards to the northwestern and southeastern margins of the complexes (Wang et al., 2004).

The characteristics of the eastern Louzidian and western Jinshan–Meilin faults are similar except for their different scales and opposite dips (southeastern and northwestern, respectively). Both faults strike NNE with dip angles of 20°–40°. From bottom to top, the faults include ~3 km thick ductile and ductile–brittle shear zone, ~100 m thick brittle chloritic breccia, ~0.5 m thick microbreccia, and fault gauges (Fig. 2a–b; Han et al., 2001; Wang et al., 2004; Wang and Zheng, 2005). Vertically, each of these structural elements was superposed on the earlier one. The eastern zone is characterised by a SE-dipping foliation and the western zone by a NW-dipping foliation, but both with a common NE-trending mineral elongation lineation. The mineral lineation, asymmetric porphyroclasts and S–C fabrics in shear zone all show a top-to-the-NE shear sense (Fig. 2a and c; Han et al., 2012; Wang et al., 2004, 2011; Zhang et al., 2002). The Rb–Sr isochron and Ar–Ar (K-feldspar, biotite and hornblende) ages for mylonitic rocks indicate that these ductile and ductile–brittle deformations were generated between ca. 135 and 125 Ma (Liu et al., 2003; Wang and Zheng, 2005; Zhang et al., 2002). The initial ductile shear indicates that it formed at a depth of 18–20 km, corresponding to epidote–amphibolite facies conditions (450–550 °C, 540 MPa) (Wang et al., 2011 and references therein). The normal faults were developed along the two ductile shear zones

and show a top-to-the-NW and SE brittle shear sense (Wang and Zheng, 2005; Wang et al., 2004, 2006). Chlorite K–Ar dating indicates that the transition from top-to-the-NE to top-to-the-NW and SE shearing began at ca. 121 Ma (Wang et al., 2006). The change of the shear sense is also supported by the provenance and paleocurrent direction analysis in the rift-basins (Wang et al., 2004). Kinematic vorticity measurements show that the Louzidian shear zone is a result of a combination of early simple-shearing and a late pure-shearing (Li et al., 2010).

## 3. Geology of the Anjiayingzi gold deposit

The Anjiayingzi gold deposit, also called the Dashuiqing or Jinchanshan gold deposit, is hosted by the Jiguanzi Quartz Monzonite and located in the footwall of the Kalaqin MCC (Figs. 1c and 2). Northeast-trending, sinistral brittle–ductile and brittle faults host the gold veins of the deposit. These faults appear to be spatially and temporally related to the regional top-to-the-NE ductile–brittle shear in the Kalaqin MCC.
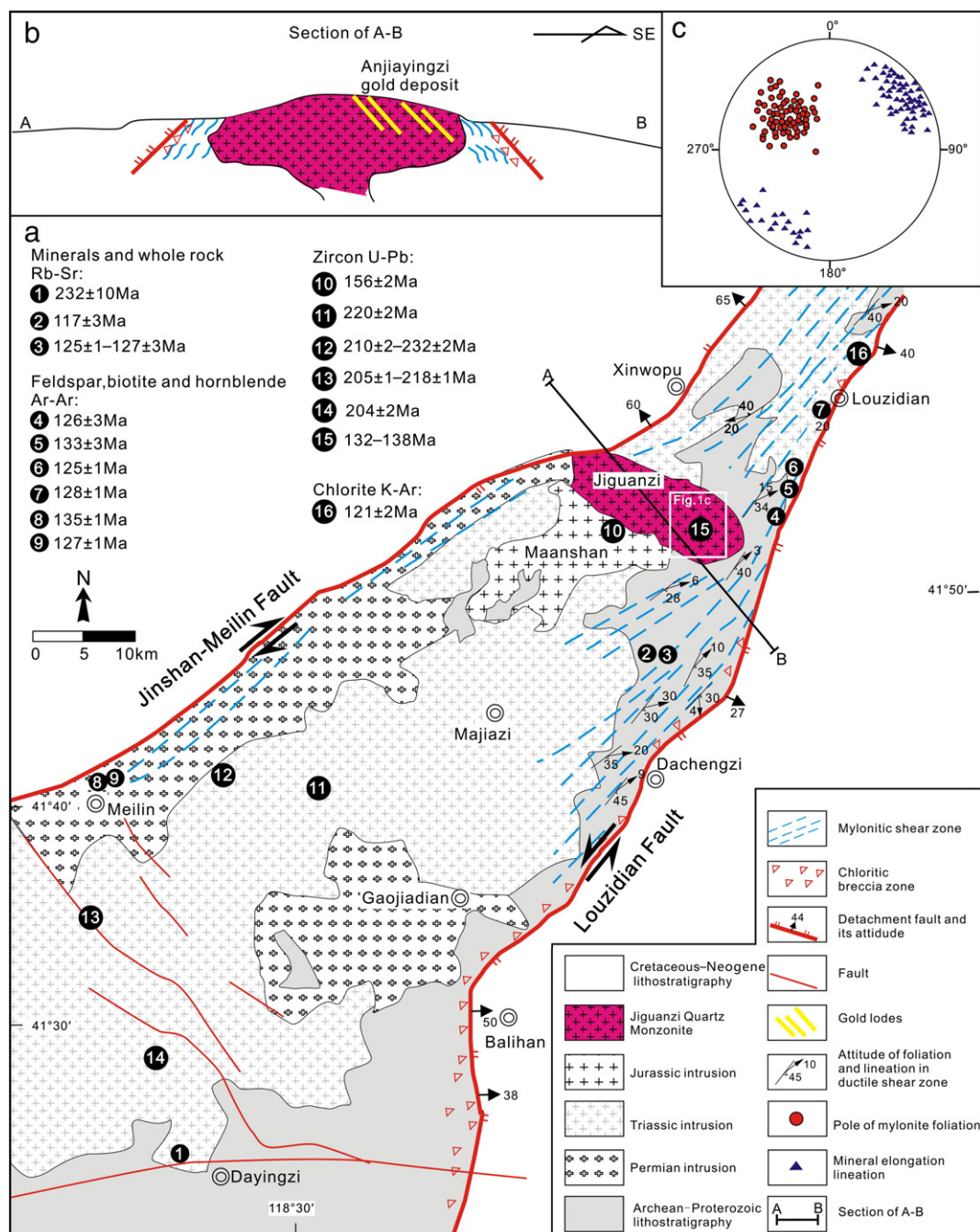


Fig. 2. The Kalaqin MCC: (a) Structural map with the available radiometric ages (Wang and Zheng, 2005); (b) cross-section for the northern Kalaqin MCC (Shao et al., 2001); and (c) equator projection of mylonite foliation and mineral elongation lineation (Han et al., 2012; Wang and Zheng, 2005). The dating methods and data source of the isotopic ages in (a) for the earlier fault (1), detachment systems (2–9 and 16), and intrusions (10–15) are: 1 — biotite, K-feldspar, plagioclase, and whole rock Rb–Sr isochron dating of the Triassic fault; 2–3 — biotite, K-feldspar, plagioclase, and whole rock Rb–Sr isochron dating of mylonitic rocks (Liu et al., 2003); 4–5 — K–feldspar and biotite Ar–Ar dating of mylonitic rocks (Zhang et al., 2002); 6–9 — biotite and hornblende Ar–Ar dating of mylonitic rocks (Wang and Zheng, 2005); 10–14 — LA–ICP–MS zircon U–Pb dating of intrusion (Ouyang, 2010); 15 — single zircon U–Pb dating for intrusion by VG 354 mass spectrometer (Li et al., 2004b); 16 — chlorite K–Ar dating of brittle chloritic breccia zone (Wang et al., 2006). The red circles and blue triangles in (c) denote the pole of mylonite foliation and lineation, respectively.

## 3.1. Country rocks, intrusive rocks, and structures

Archean biotite–plagioclase gneiss, hornblende–plagioclase gneiss and subordinate marble that are assigned to the Jianping Group host the Anjiayingzi gold deposit and the elliptical medium- to coarse-grained Jiguanzi Quartz Monzonite, which is also called the Anjiayingzi Granite (Fig. 2a). The monzonite is grey to pink in colour and consists of plagioclase (26–33 vol.%), perthitic K-feldspar (30–40 vol.%), quartz (10–15 vol.%), biotite (4–6 vol.%) and amphibole (3–5 vol.%), with minor amounts of Fe–Ti oxides, zircon, titanite and apatite. The plagioclase forms subhedral laths with occasional albite and Carlsbad–albite combined twinning, amphibole and biotite are often subhedral to euhedral, and magmatic enclaves with heterogranular texture in the pluton are ubiquitous. In addition, rhyolite dykes hosted by NE-trending mineralized fault zones are widely distributed in the eastern Nandawa and Loufengmao (Figs. 1c and 3b). Field observation shows that most of the dykes cut the orebodies, but some of them are also pyritized, suggesting that the emplacement of dykes is at least slightly younger than the gold mineralization.

Abundant brittle and brittle–ductile faults are up to several kilometres long, and up to ~40 m wide (Figs. 1c and 3). The faults are commonly en-echelon (Fig. 3c–d), trend northeast and dip 30°–65° SE.

A few N-trending and steep tensional mineralized fractures are developed in the Laohudonggou and Anjiayingzi. The orientations of the fault sets are indicative of a regional sinistral shear displacement with a principal compressional stress direction of NNW–SSE. This sinistral shear sense spatially and temporally coincides with the regional top-to-the-NE ductile–brittle shear at the Kalaqin MCC. This observation is consistent with previous structural studies in the region (Fang and Tong, 1995; Trumbull et al., 1996). Moreover, all of the faults cut the Early Cretaceous Jiguanzi Quartz Monzonite and are locally intruded by the rhyolite dykes, especially in the Nandawa–Loufengmao area (Fig. 3b).

## 3.2. Mineralization and alteration

The economically significant orebodies at Anjiayingzi were discovered between 1979 and 1996, and are presently being mined underground. The total reserves measured in the late 1990s were 1.32 Mt at 13.9 g/t Au, with bonanza clusters of up to 769 g/t Au in the Nandawa area (Fig. 1c; Li, 2000).

The gold veins at Anjiayingzi are controlled by NE-trending faults, and almost exclusively hosted by the Jiguanzi Quartz Monzonite. The contact between gold veins and wall rocks is sharp, although the hydrothermal
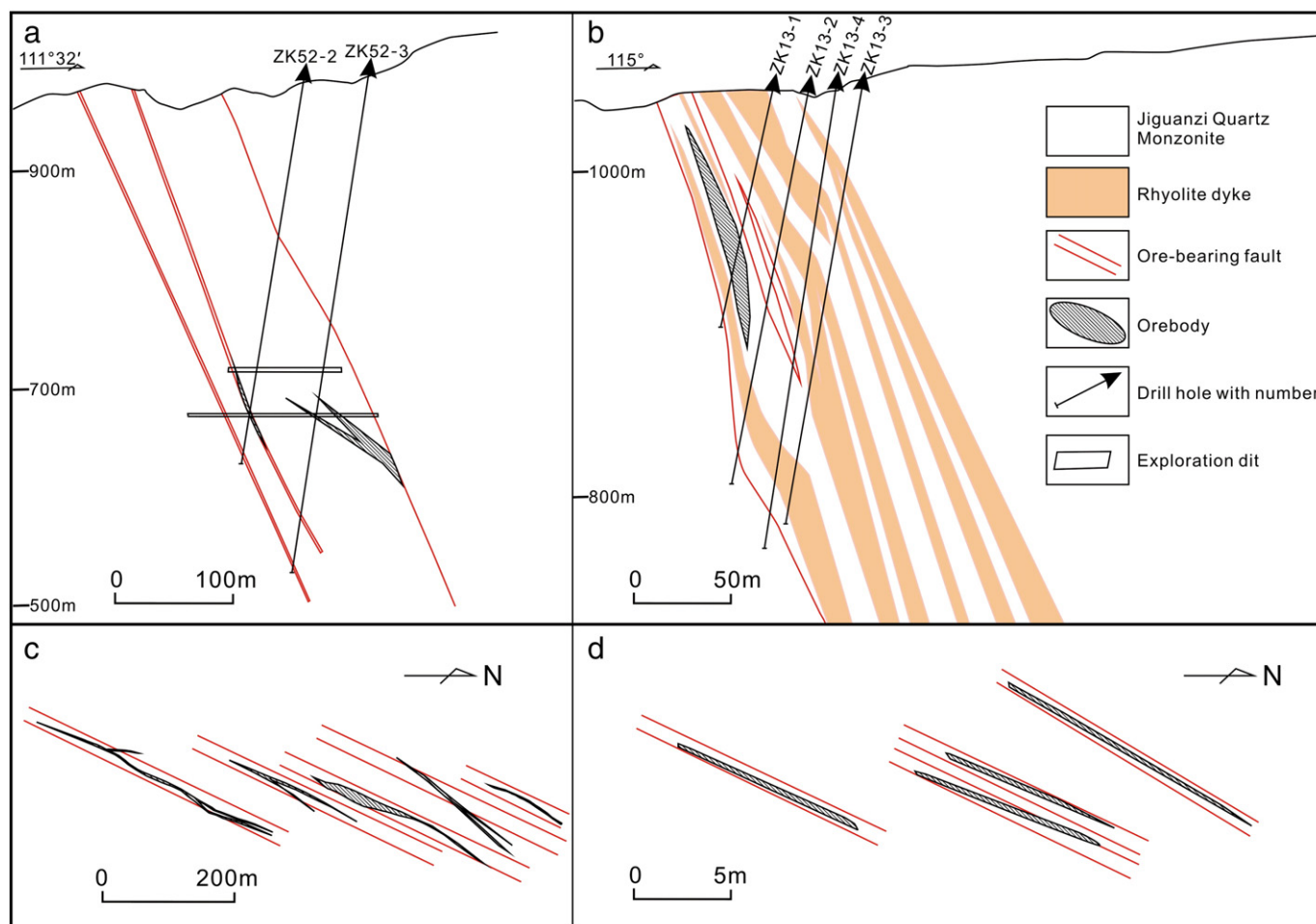


**Fig. 3.** The western 52 (a) and eastern 13 (b) cross-sections showing the occurrence and morphology of major gold veins at the Anjiayingzi gold deposit. Parts (c) and (d) illustrate the geometric and textural features of the Western and Eastern gold veins hosted by faults in the Jiguanzi Quartz Monzonite; and they are located in the 632 m level at the Yangpo and 945 m level at the Loufengmao, respectively.

**Fig. 4.** Photographs (a–b) and reflected-light photomicrographs (c–h) of ore from the Anjiayingzi gold deposit: (a) the Western gold ore; (b) the Eastern disseminated mineralization; (c) typical morphology and texture of the pyrite in the gold ore; (d–f) assemblages of polymetallic sulphide minerals in the major metallogenic stage; (g) occurrence and morphology of native gold; and (h) supergene sulphide minerals. Abbreviations: Py — pyrite, Ccp — chalcopyrite, Gn — galena, Au — native gold, Qz — quartz, Cv — covellite, Mal — malachite, Chl — chlorite.
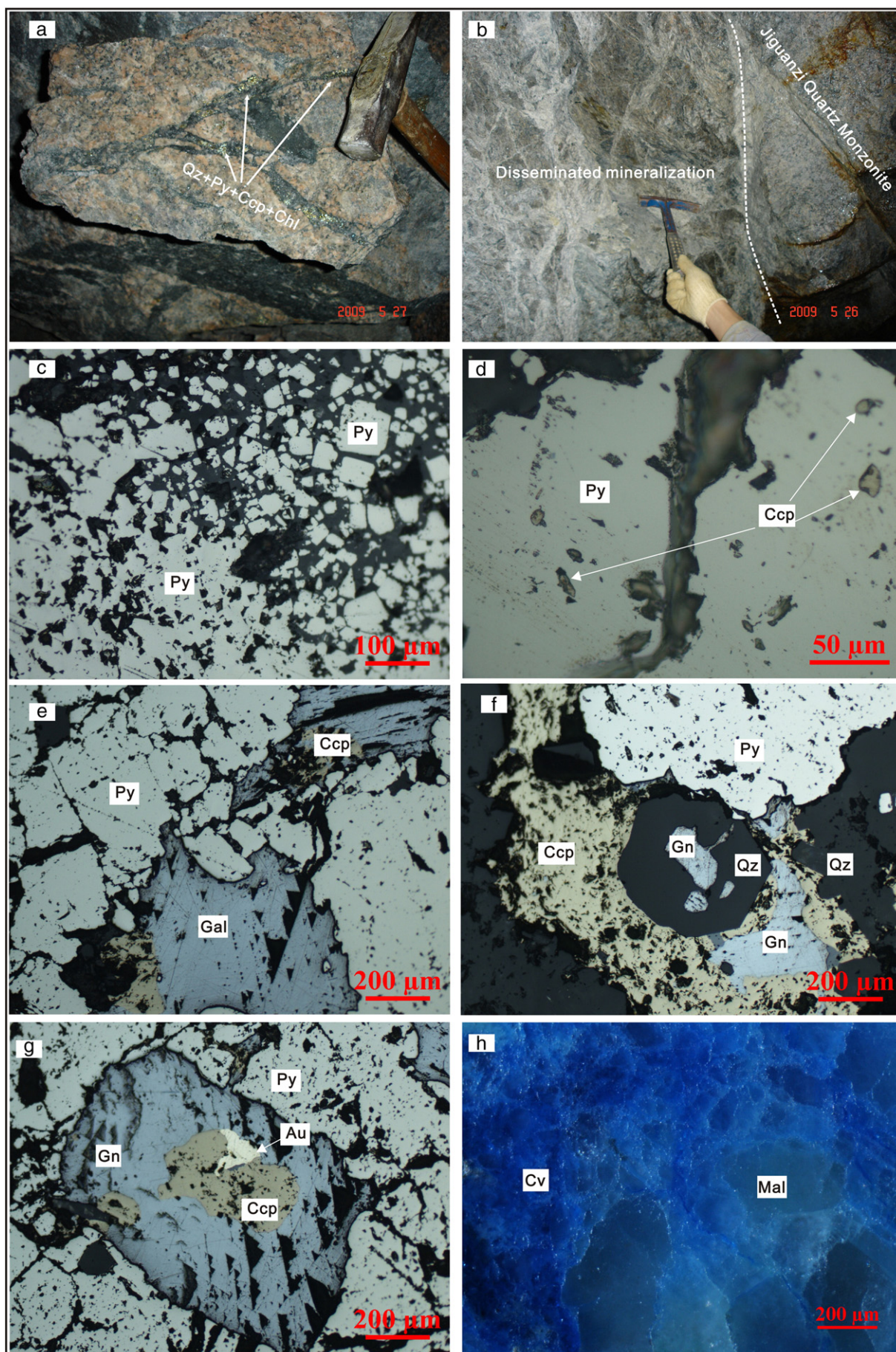
alteration halos may develop outside of the main veins (Fig. 4a–b). These gold veins can be divided into two parts spatially: the Western and Eastern veins (Fig. 1c). The Western veins are located around the Laohudonggou and Yangpo, with mineralized zones commonly trending 015°–035° and dipping 40°–60° SE (Figs. 1c and 3a). Single veins of them extend for ca. 70 to 450 m along strike with a width of 0.4 to 1.5 m and continue ca. 10 to 80 m downplunge (Fig. 3a and c). These veins are hosted by brittle fractures, and they consist of en-echelon auriferous quartz–sulphide veins (Fig. 4a) that are parallel to faults spaced ~40–70 m apart (Fig. 3c). The Eastern veins are located in the Nandawa and Loufengmao dominantly where they are hosted by a ~6 km long fault trending 025°–030° NE and dipping 55°–65° SE (Figs. 1c and 3b). Single veins of them extend for ca. 10 m to more than 400 m along strike and continue 10 to 200 m downplunge, with width of 0.5 to 7.6 m (Fig. 3b and d). The Eastern veins hosted by the brittle–ductile faults are also locally en-echelon (Fig. 3d), and consist of disseminated mineralization with subordinate quartz–sulphide veins (Fig. 4b). Although the ore-bearing faults hosting the Western and Eastern gold veins are different, all mineralization developed preferentially in the dilational jogs and changes along strike within the fault zones.

The auriferous quartz–sulphide veins from the Western veins contain 4–30 vol.% sulphides including pyrite and minor amounts of chalcopyrite, galena, sphalerite and rare molybdenite. In contrast, the veins in the Eastern area only contain small amounts of sulphides (Figs. 4a–g and 5a–c). Secondary malachite and covellite are common in the surface portion of the major veins (Fig. 4h), and minor amounts of tetradymite, boulangerite and pyrrhotite have been reported in the Anjiayingzi deposit (Trumbull et al., 1996).

Two types of pyrite have been recognized. The first type is euhedral to subhedral, coarse-grained with a crystal diameter of up to 5 mm, forming isolated crystals; this type is typically micro-fractured and filled with chalcopyrite, galena and sphalerite (Fig. 4d–g). The second type is commonly euhedral, fine-grained and forms cubes with a diameter of up to 100 μm (Fig. 4c). Native gold and electrum (5–100 μm) is present in microfractures where pyrite, chalcopyrite, galena and sphalerite co-exist (Fig. 4g). Gold fineness, determined by SEM-EDS microanalysis, is in the range of 700–850. The veins from Anjiayingzi contain several percent base-metal, and have low Au/Ag ratios (<1) and arsenic content (<54 ppm) with rare arsenopyrite (Trumbull et al., 1996). These characteristics are different from typical orogenic gold deposits from other terranes in the world (Goldfarb et al., 2005).

Hydrothermal alteration halos are well developed around the gold veins with width of several centimetres to the metre scale. The assemblages of K-feldspar, albite, quartz and sericite were formed during the early stage of alteration. They are distal to the auriferous veins or locally captured or cut by the later epidote–chlorite assemblages and quartz–sulphide veins (Fig. 5a–d). Sericite is commonly an alteration product of plagioclase and K-feldspar in the wall rock (Fig. 5e). An assemblage of chlorite–epidote (–sericite) is developed proximal to the quartz–sulphide veins and overprints the earlier stage assemblages of K-feldspar–albite–quartz (Fig. 5c–e). Calcite, ankerite, and minor amounts of quartz crystallized in the latest stage of alteration and overprinted the earlier alteration assemblages (Fig. 5d). Mass-balance calculations indicate that the hydrothermal alteration may have removed Na, Ca, Sr and Ba from the Jiguanzi Quartz Monzonite host, and added Mn, K, Rb, S, $CO_2$, Au, Cu, Pb and Zn (Trumbull et al., 1996).

Based on the mineralogy and textural relationships described above, the following hypogene stages are recognized in the mineralization process: (1) quartz–coarse-grained pyrite; (2) quartz–fine-grained pyrite; (3) quartz–polymetallic sulphides; and (4) quartz–carbonate.

## 4. Sampling and analytical methods

Sample JY1 was collected from the Yangpo area for geochronological and geochemical studies (Fig. 1c). Zircons were extracted from the sample using the density and magnetic separation technique at the laboratory of Langfang Regional Geological Survey Institute in the Hebei Province of China. Cathodoluminescence (CL) images were obtained in the electron microprobe laboratory at the State Key Laboratory of Geological Processes and Mineral Resources (GPMR), China University of Geosciences (CUG), Wuhan. Zircon U–Pb dating and trace element analyses were conducted synchronously using a laser ablation inductively coupled plasma mass spectrometry (LA–ICP–MS) at GPMR with a spot size of 32 μm. Laser sampling was performed using a 193-nm GeoLas 2005. An Agilent 7500a inductively coupled plasma mass spectrometry (ICP–MS) instrument was used to acquire ion-signal intensities. Each analysis incorporated a background acquisition of approximately 20–30 s (gas blank) followed by 50 s of data acquisition from the sample. Zircon 91500 was used as an external standard for U–Pb dating and was analysed twice every five analyses. Detailed operating conditions for the laser ablation system and the ICP–MS instrument are the same as described by Liu et al. (2008, 2010). *ICPMSDataCal* was used for off-line selection and integration of background and analytical signals, and time-drift correction and quantitative calibration for trace element analyses and U–Pb dating (Liu et al., 2008, 2010). Concordia diagrams and weighted mean calculations were made using Isoplot Version 3 (Ludwig, 2003).

All electron probe microanalyses (EPMA) of hornblende and plagioclase were carried out at GPMR with a JEOL JXA-8100 Superprobe. The operating settings were at a 15 kV accelerating voltage, 20 nA beam current, and 1 μm beam diameter. The sample locations for JY1 and JY7, used in EPMA, are illustrated in Fig. 1c. The Jiguanzi Quartz Monzonite contains quartz, plagioclase, hornblende, K-feldspar, biotite and Fe–Ti oxides, so the amphibole–plagioclase thermometry and aluminium-in-hornblende barometry are effective ways to estimate its crystallization temperature and pressure. Aluminium-in-hornblende barometry has also been widely used to calculate the depth of emplacement for granites (Anderson and Smith, 1995; Anderson et al., 2008; Zhang and Zhao, 2013). The crystallization temperatures for the monzonite were calculated using the plagioclase–hornblende geothermometer of Holland and Blundy (1994), and the pressures were calculated using the barometer of Schmidt (1992) and Anderson and Smith (1995). Emplacement depths were calculated based on the assumption that average crustal density of the northern NCC was 2.9 g/cm³ (Zhang and Zhao, 2013).

Microthermometric measurements of fluid inclusion were performed at the Faculty of Earth Resources, CUG, using a Linkam THM600 heating–freezing stage and a Leica MD2500 P microscope. Freezing experiments were performed firstly on all sections to avoid inclusion rupture. The estimated accuracy was ±0.1 °C at temperatures below 30 °C and ±1 °C at temperatures above 30 °C. Salinities of two-phase fluid inclusions, expressed as wt.% NaCl equiv., were calculated using the MacFlincor computer software (Brown and Hagemann, 1995). Fluid inclusion study was conducted on samples from the Yangpo and Nandawa mining areas. The samples are collected from the Western quartz–sulphides veins and Eastern disseminated ores. Thus, the results from microthermometric measurements are typical representatives of the major mineralization stage.

## 5. Results

### 5.1. Zircon U–Pb geochronology of the Jiguanzi Quartz Monzonite

Trace element assays, U–Pb isotope compositions and CL images for zircons from the Jiguanzi Quartz Monzonite are presented in Table 1 and Fig. 6. Zircon grains extracted from Sample JY1 are transparent, colourless to light yellow and dominated by short-, long-prismatic shapes. Their lengths range from 40 to 400 μm with aspect ratios of ~1:1 to 6:1. All zircon grains display clear oscillatory zoning in the CL images and high Th/U ratios (0.55–0.80), indicative of a magmatic origin (Fig. 6).
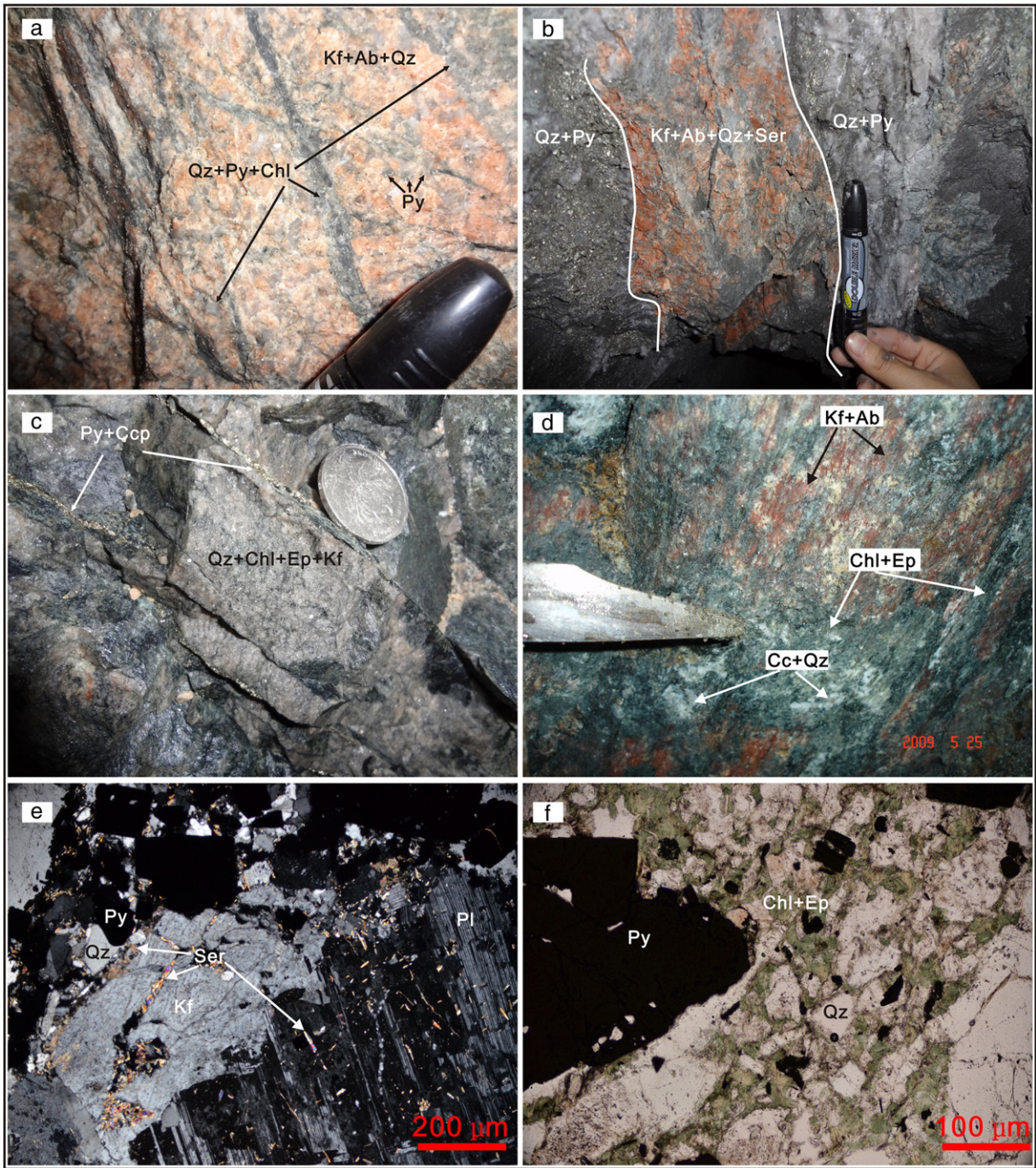
**Fig. 5.** Photographs (a–d) and transmitted-light photomicrographs (e–f) of alteration assemblages associated with gold mineralization showing: (a–c) early K-feldspar and albite alteration assemblages with minor quartz, which were overprinted by auriferous quartz–sulphide (–chlorite) veins; (d) early K-feldspar and associated alteration assemblages overprinted by the later chlorite–epidote–calcite alteration; (e) sericite locally replacing plagioclase and K-feldspar, and forms thin veinlets with quartz–pyrite filling in fractures; and (f) alteration assemblages of chlorite–epidote–quartz–pyrite. Abbreviations: Kf — K-feldspar, Qz — quartz, Chl — chlorite, Ep — epidote, Cc — calcite, Ser — sericite, Pl — plagioclase, Py — pyrite, Ccp — chalcopyrite.

Thirteen spots on twelve zircon grains were measured. Single zircon U–Pb dating reveals a population of ca. 136–131 Ma. They are nearly concordant and yield a weighted mean $^{206}Pb/^{238}U$ age of ca. 133 ± 1 Ma (MSWD = 1.1; n = 13). Previous zircon U–Pb dating for this intrusion by VG 354 mass spectrometer gave weighted $^{206}Pb/^{238}U$ ages of ca. 138 ± 1 and ca. 132 ± 5 Ma (Li et al., 2004b), which are similar in age to our date, and the age of the Jiguanzi Quartz Monzonite is taken as being ca. 133 Ma.

### 5.2. Mineral chemistry and temperature–pressure–depth estimates for the Jiguanzi Quartz Monzonite

The representative EPMA results of hornblende and plagioclase are listed in Tables 2 and 3, and plotted in Fig. 7. Structural formulae calculations for hornblende are based on 23 oxygens following the method of Holland and Blundy (1994). For all hornblende analysed, the $Ca_B$ (B-site; apfu — atoms per formula unit) is higher than 1.50 apfu, $Ca_A$

**Table 1**
LA–ICP-MS zircon U–Pb dating data for JY1-1 from the Jiguanzi Quartz Monzonite.

| Spot number | Th ppm | U ppm | Th/U | U–Th–Pb isotopic ratio | | | | | | | | Age (Ma) | | | | | | | |
|---|---|---|---|---|---|---|---|---|---|---|---|---|---|---|---|---|---|---|---|
| | | | | $^{207}Pb/^{206}Pb$ | 1σ | $^{207}Pb/^{235}U$ | 1σ | $^{206}Pb/^{238}U$ | 1σ | $^{208}Pb/^{232}Th$ | 1σ | $^{207}Pb/^{206}Pb$ | 1σ | $^{207}Pb/^{235}U$ | 1σ | $^{206}Pb/^{238}U$ | 1σ | $^{208}Pb/^{232}Th$ | 1σ |
| JY1-1-1 | 187.83 | 280.15 | 0.67 | 0.0515 | 0.0026 | 0.1485 | 0.0072 | 0.0211 | 0.0002 | 0.0066 | 0.0002 | 265 | 117 | 141 | 6 | 135 | 2 | 133 | 4 |
| JY1-1-2 | 178.49 | 325.99 | 0.55 | 0.0591 | 0.0023 | 0.1743 | 0.0071 | 0.0214 | 0.0002 | 0.0074 | 0.0002 | 569 | 87 | 163 | 6 | 136 | 1 | 148 | 5 |
| JY1-1-3 | 619.81 | 785.79 | 0.79 | 0.0504 | 0.0010 | 0.1450 | 0.0030 | 0.0209 | 0.0001 | 0.0063 | 0.0001 | 213 | 46 | 137 | 3 | 133 | 1 | 127 | 2 |
| JY1-1-4 | 306.24 | 515.47 | 0.59 | 0.0481 | 0.0013 | 0.1386 | 0.0037 | 0.0210 | 0.0002 | 0.0063 | 0.0002 | 106 | 63 | 132 | 3 | 134 | 1 | 128 | 3 |
| JY1-1-5 | 171.63 | 215.73 | 0.80 | 0.0490 | 0.0019 | 0.1398 | 0.0052 | 0.0211 | 0.0002 | 0.0064 | 0.0002 | 150 | 93 | 133 | 5 | 134 | 1 | 129 | 3 |
| JY1-1-6 | 579.18 | 818.47 | 0.71 | 0.0481 | 0.0010 | 0.1379 | 0.0030 | 0.0209 | 0.0001 | 0.0063 | 0.0001 | 106 | 50 | 131 | 3 | 134 | 1 | 127 | 2 |
| JY1-1-7 | 424.90 | 574.11 | 0.74 | 0.0507 | 0.0013 | 0.1445 | 0.0035 | 0.0209 | 0.0001 | 0.0063 | 0.0001 | 228 | 59 | 137 | 3 | 133 | 1 | 127 | 3 |
| JY1-1-8 | 337.10 | 419.32 | 0.80 | 0.0499 | 0.0018 | 0.1411 | 0.0048 | 0.0207 | 0.0002 | 0.0062 | 0.0001 | 191 | 83 | 134 | 4 | 132 | 1 | 126 | 3 |
| JY1-1-9 | 552.66 | 757.80 | 0.73 | 0.0601 | 0.0034 | 0.1731 | 0.0095 | 0.0210 | 0.0002 | 0.0072 | 0.0002 | 606 | 122 | 162 | 8 | 134 | 2 | 146 | 7 |
| JY1-1-10 | 540.78 | 725.82 | 0.75 | 0.0529 | 0.0013 | 0.1516 | 0.0035 | 0.0210 | 0.0004 | 0.0067 | 0.0003 | 324 | 28 | 143 | 3 | 134 | 1 | 134 | 3 |
| JY1-1-11 | 264.42 | 340.67 | 0.78 | 0.0561 | 0.0040 | 0.1631 | 0.0107 | 0.0211 | 0.0004 | 0.0071 | 0.0004 | 457 | 161 | 153 | 9 | 135 | 3 | 143 | 6 |
| JY1-1-12 | 407.32 | 643.19 | 0.63 | 0.0487 | 0.0014 | 0.1376 | 0.0037 | 0.0205 | 0.0001 | 0.0064 | 0.0001 | 200 | 60 | 131 | 3 | 131 | 1 | 129 | 3 |
| JY1-1-13 | 629.41 | 819.60 | 0.77 | 0.0523 | 0.0017 | 0.1501 | 0.0043 | 0.0210 | 0.0001 | 0.0065 | 0.0001 | 298 | 68 | 142 | 4 | 134 | 1 | 131 | 2 |
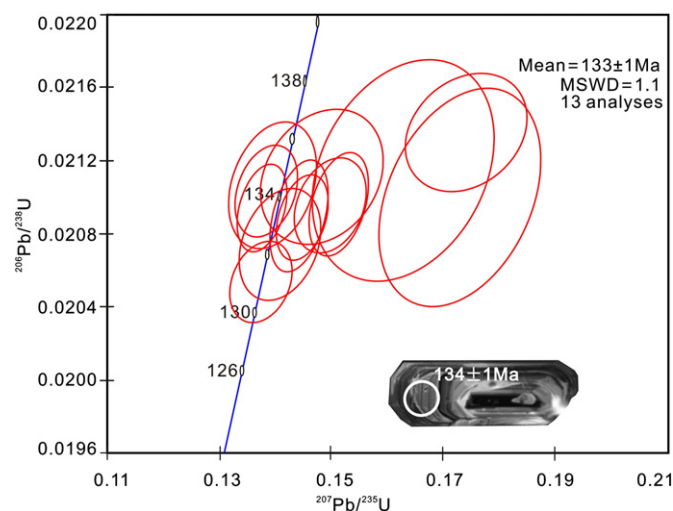


**Fig. 6.** U–Pb Concordia plots for zircons from the Jiguanzi Quartz Monzonite. The inset1 illustrates the representative zircon CL image, site of LA–ICP-MS U–Pb analysis and corresponding $^{206}Pb/^{238}U$ ages. MSWD: mean square of weighted deviation.

(A-site; apfu) is lower than 0.50 apfu, and the $(Na + K)_A$ is also lower than 0.50 apfu (Table 2). Thus they can be classified as magnesiohornblende following the nomenclature of Leake et al. (1997) (Fig. 7). Structural formulae for plagioclase were calculated on the basis of 8 oxygens and 5 cations. The values for anorthite (An) range from 15.2 to 24.3, and that for albite (Ab) ranges from 72.4 to 81.9 (Table 3).

Temperature–pressure–depth estimate results are presented in Table 4. The crystallization temperatures, calculated using the geothermometer A ($T_{ed-tr}$ — $T_{edenite-tremolite}$) and B ($T_{ed-ri}$ — $T_{edenite-richterite}$) of Holland and Blundy (1994) range between 691 and 759 °C and between 640 and 691 °C, respectively. Because the $T_{ed-ri}$ using geothermometer B is considered more accurate in estimating temperatures (Anderson et al., 2008), we take the $T_{ed-ri}$ range of 640 to 691 °C as the crystallization temperatures for the Jiguanzi Quartz Monzonite. The pressures calculated using the $P_{AS}$ barometer of Anderson and Smith (1995) range from 167 to 271 MPa with an average of 245 MPa, which is nearly the same within error as the mean of 235 MPa using the $P_{Sch}$ barometer of Schmidt (1992). The barometer of Anderson and Smith (1995) was adopted in this study, because of its consideration of the influence of temperature and oxygen fugacity on pressure calculations. Based on the results described above, the monzonite is estimated to have been emplaced at a depth of between 5.9 and 9.5 km (i.e. an average depth of 8.6 km).

*5.3. Petrography and microthermometry of fluid inclusions*

Primary fluid inclusions from the Anjiayingzi deposit form isolated or groups of inclusions with various shapes (Fig. 8a). The four types of inclusions identified are: (1) two-phase liquid-rich fluid inclusions (V–L-type; Fig. 8); (2) three-phase carbonic fluid inclusions (C-type; Fig. 8b); (3) daughter mineral-bearing saline fluid inclusions (H-type; Fig. 8c); and (4) two-phase vapour-rich fluid inclusions (V-type).

The V–L-type fluid inclusions consist of a vapour bubble and a liquid phase. They have regular to irregular shapes and range from 3 to 30 μm in size. The vapour phase normally occupies between 5 and 50 vol.%. The V–L-type inclusions are widespread in the quartz–polymetallic sulphide veins and disseminated ores.

The C-type fluid inclusions consist of three phases at room temperature (liquid $H_2O$ + liquid $CO_2$ + vapour $CO_2$) with 20–40 vol.% carbonic liquid and vapour phases of total volume. The C-type inclusions are generally 20 to 35 μm in diameter, and have elliptic or negative crystal shapes. They are commonly developed around the V–L-type inclusions, but are much less abundant.

**Table 2**
Representative hornblende compositions of the Jiguanzi Quartz Monzonite.

| Sample spot | JY7-1-13 | JY7-1-14 | JY7-1-15 | JY7-1-16 | JY7-2-14 | JY7-2-15 | JY7-2-16 | JY7-2-17 | JY1-1-9 | JY1-1-10 | JY1-1-11 |
|---|---|---|---|---|---|---|---|---|---|---|---|
| $SiO_2$ | 47.17 | 47.57 | 47.55 | 47.17 | 47.29 | 47.56 | 47.18 | 48.71 | 49.68 | 47.76 | 46.61 |
| $TiO_2$ | 1.06 | 1.20 | 1.24 | 1.25 | 1.31 | 1.30 | 1.00 | 0.99 | 0.56 | 1.10 | 1.15 |
| $Al_2O_3$ | 6.47 | 6.61 | 6.63 | 6.67 | 6.87 | 6.74 | 6.51 | 5.60 | 4.87 | 6.33 | 6.65 |
| $Cr_2O_3$ | 0.00 | 0.00 | 0.00 | 0.00 | 0.00 | 0.00 | 0.00 | 0.00 | 0.04 | 0.00 | 14.75 |
| FeO | 16.01 | 15.77 | 15.43 | 15.29 | 15.93 | 15.99 | 14.93 | 14.15 | 14.67 | 15.35 | 13.07 |
| MgO | 12.61 | 12.03 | 12.12 | 12.57 | 12.49 | 12.73 | 13.04 | 14.13 | 13.68 | 12.82 | 0.47 |
| MnO | 0.52 | 0.43 | 0.61 | 0.52 | 0.48 | 0.60 | 0.58 | 0.54 | 0.56 | 0.54 | 11.83 |
| CaO | 12.02 | 12.09 | 12.01 | 11.71 | 11.78 | 11.48 | 11.74 | 12.20 | 12.19 | 11.91 | 1.68 |
| $Na_2O$ | 1.08 | 1.23 | 1.26 | 1.36 | 1.35 | 1.36 | 1.49 | 1.28 | 0.85 | 1.25 | 0.66 |
| $K_2O$ | 0.52 | 0.58 | 0.58 | 0.61 | 0.61 | 0.61 | 0.66 | 0.53 | 0.34 | 0.56 | 0.00 |
| Total | 97.44 | 97.49 | 97.40 | 97.12 | 98.08 | 98.34 | 97.11 | 98.11 | 97.42 | 97.61 | 96.87 |
| *Formulae per Holland and Blundy (1994)* | | | | | | | | | | | |
| *T site* | | | | | | | | | | | |
| Si | 6.948 | 7.036 | 7.031 | 6.978 | 6.914 | 6.944 | 6.975 | 7.088 | 7.087 | 7.000 | 6.924 |
| $Al^{IV}$ | 1.052 | 0.964 | 0.969 | 1.022 | 1.086 | 1.056 | 1.025 | 0.912 | 0.913 | 1.000 | 1.076 |
| *C site* | | | | | | | | | | | |
| $Al^{VI}$ | 0.072 | 0.188 | 0.187 | 0.141 | 0.089 | 0.105 | 0.110 | 0.048 | 0.158 | 0.122 | 0.089 |
| Ti | 0.117 | 0.133 | 0.137 | 0.139 | 0.140 | 0.142 | 0.111 | 0.108 | 0.113 | 0.127 | 0.128 |
| $Fe^{3+}$ | 0.557 | 0.267 | 0.277 | 0.376 | 0.471 | 0.496 | 0.399 | 0.368 | 0.323 | 0.393 | 0.354 |
| Mg | 2.769 | 2.651 | 2.671 | 2.772 | 2.793 | 2.769 | 2.873 | 3.064 | 2.784 | 2.794 | 2.892 |
| Mn | 0.065 | 0.054 | 0.076 | 0.065 | 0.043 | 0.074 | 0.072 | 0.067 | 0.081 | 0.066 | 0.059 |
| $Fe^{2+}$ | 1.415 | 1.683 | 1.631 | 1.508 | 1.459 | 1.414 | 1.435 | 1.345 | 1.532 | 1.491 | 1.478 |
| Ca | 0.005 | 0.024 | 0.022 | 0.000 | 0.004 | 0.000 | 0.000 | 0.000 | 0.008 | 0.007 | 0.000 |
| *B site* | | | | | | | | | | | |
| $Fe^{2+}$ | 0.000 | 0.000 | 0.000 | 0.007 | 0.000 | 0.042 | 0.012 | 0.008 | 0.000 | 0.008 | 0.001 |
| Ca | 1.891 | 1.891 | 1.881 | 1.856 | 1.890 | 1.795 | 1.860 | 1.902 | 1.875 | 1.871 | 1.883 |
| Na | 0.109 | 0.109 | 0.119 | 0.137 | 0.110 | 0.163 | 0.128 | 0.089 | 0.125 | 0.121 | 0.116 |
| *A site* | | | | | | | | | | | |
| Ca | 0.000 | 0.000 | 0.000 | 0.000 | 0.000 | 0.000 | 0.000 | 0.000 | 0.000 | 0.000 | 0.000 |
| Na | 0.198 | 0.244 | 0.241 | 0.251 | 0.246 | 0.221 | 0.298 | 0.271 | 0.213 | 0.243 | 0.368 |
| K | 0.098 | 0.108 | 0.108 | 0.114 | 0.110 | 0.113 | 0.125 | 0.098 | 0.117 | 0.110 | 0.125 |
| Al (total) | 0.659 | 0.600 | 0.610 | 0.651 | 0.648 | 0.680 | 0.672 | 0.697 | 0.681 | 0.655 | 0.712 |

The saline H-type fluid inclusions contain three phases, i.e., a vapour bubble, a brine liquid, and a solid phase, generally with variable filling degree and elliptic or negative crystal shapes. The solid phase is commonly composed of halite crystals. H-type inclusions are 10 to 20 μm in diameter and often accompanied by the V–L-type and C-type inclusions.

The V-type fluid inclusions consist of a vapour bubble and a liquid phase with high filling degree (>50 vol.%), negative crystal shapes and

**Table 3**
Representative plagioclase compositions of the Jiguanzi Quartz Monzonite.

| Sample spot | JY7-1-13 | JY7-1-14 | JY7-1-15 | JY7-1-16 | JY7-2-14 | JY7-2-15 | JY7-2-16 | JY7-2-17 | JY1-1-9 | JY1-1-10 | JY1-1-11 |
|---|---|---|---|---|---|---|---|---|---|---|---|
| $SiO_2$ | 63.83 | 63.32 | 63.50 | 63.63 | 65.30 | 65.63 | 65.98 | 64.15 | 64.43 | 64.67 | 62.28 |
| $TiO_2$ | 0.00 | 0.00 | 0.00 | 0.00 | 0.00 | 0.00 | 0.00 | 0.00 | 0.00 | 0.00 | 0.00 |
| $Al_2O_3$ | 21.81 | 22.79 | 22.86 | 22.18 | 21.21 | 21.44 | 22.24 | 22.48 | 22.64 | 23.37 | 24.01 |
| $Cr_2O_3$ | 0.00 | 0.00 | 0.00 | 0.00 | 0.01 | 0.00 | 0.00 | 0.00 | 0.00 | 0.00 | 0.00 |
| FeO | 0.08 | 0.07 | 0.10 | 0.06 | 0.05 | 0.13 | 0.08 | 0.08 | 0.11 | 0.14 | 0.11 |
| MgO | 0.00 | 0.00 | 0.00 | 0.00 | 0.00 | 0.00 | 0.00 | 0.00 | 0.00 | 0.00 | 0.00 |
| MnO | 0.00 | 0.00 | 0.01 | 0.00 | 0.00 | 0.00 | 0.00 | 0.00 | 0.00 | 0.00 | 0.00 |
| CaO | 3.24 | 4.24 | 4.35 | 3.78 | 3.13 | 3.10 | 3.36 | 3.63 | 3.92 | 4.46 | 5.14 |
| $Na_2O$ | 9.65 | 8.47 | 8.70 | 8.99 | 9.05 | 9.20 | 9.04 | 9.30 | 8.92 | 7.42 | 8.56 |
| $K_2O$ | 0.54 | 0.56 | 0.20 | 0.33 | 0.41 | 0.56 | 0.64 | 0.66 | 0.60 | 0.57 | 0.42 |
| Total | 99.15 | 99.45 | 99.72 | 98.97 | 99.17 | 100.06 | 101.34 | 100.29 | 100.61 | 100.61 | 100.51 |
| *Number of ions on the basis of 8 oxygens* | | | | | | | | | | | |
| Si | 2.845 | 2.813 | 2.811 | 2.836 | 2.893 | 2.887 | 2.867 | 2.829 | 2.829 | 2.826 | 2.750 |
| Al | 1.146 | 1.193 | 1.193 | 1.165 | 1.108 | 1.112 | 1.139 | 1.168 | 1.172 | 1.203 | 1.249 |
| Ti | 0.000 | 0.000 | 0.000 | 0.000 | 0.000 | 0.000 | 0.000 | 0.000 | 0.000 | 0.000 | 0.000 |
| Cr | 0.000 | 0.000 | 0.000 | 0.000 | 0.001 | 0.000 | 0.000 | 0.000 | 0.000 | 0.000 | 0.000 |
| Mn | 0.000 | 0.000 | 0.000 | 0.000 | 0.000 | 0.000 | 0.000 | 0.000 | 0.000 | 0.000 | 0.000 |
| Mg | 0.000 | 0.000 | 0.000 | 0.000 | 0.000 | 0.000 | 0.000 | 0.000 | 0.000 | 0.000 | 0.000 |
| $Fe^{2+}$ | 0.003 | 0.003 | 0.004 | 0.002 | 0.002 | 0.005 | 0.003 | 0.003 | 0.004 | 0.005 | 0.004 |
| Ca | 0.155 | 0.202 | 0.206 | 0.180 | 0.149 | 0.146 | 0.156 | 0.171 | 0.184 | 0.209 | 0.243 |
| Na | 0.834 | 0.729 | 0.747 | 0.777 | 0.777 | 0.785 | 0.761 | 0.795 | 0.759 | 0.629 | 0.732 |
| K | 0.031 | 0.032 | 0.011 | 0.019 | 0.023 | 0.031 | 0.035 | 0.037 | 0.033 | 0.031 | 0.023 |
| *Mol%* | | | | | | | | | | | |
| Or | 3.0 | 3.3 | 1.2 | 1.9 | 2.5 | 3.3 | 3.7 | 3.7 | 3.4 | 3.6 | 2.3 |
| Ab | 81.8 | 75.7 | 77.5 | 79.6 | 81.9 | 81.6 | 79.9 | 79.2 | 77.7 | 72.4 | 73.3 |
| An | 15.2 | 20.9 | 21.4 | 18.5 | 15.7 | 15.2 | 16.4 | 17.1 | 18.9 | 24.0 | 24.3 |
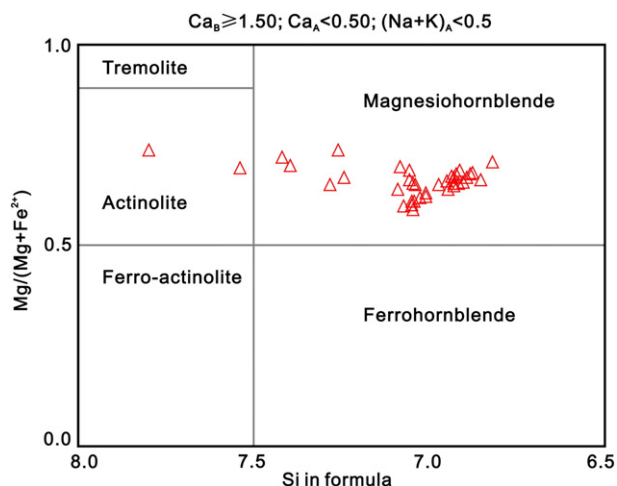
**Fig. 7.** Hornblende classification (after Leake et al., 1997). Data are from Table 2 and our unpublished data (Fu Lebing, unpublished data).

diameter of 6 to 10 μm. These inclusions are often present in quartz formed during the earlier stage of mineralization (Li et al., 2004a).

The microthermometric characteristics of the different types of fluid inclusions are described below and the associated data are summarized in Table 5 and Fig. 9. The melting temperatures of the carbonic phase ($Tm_{CO_2}$) range from −60.4 to −56.6 °C and cluster at −56.6 to −57.2 °C, indicating that there are little or no impurities in the $CO_2$ phase (Table 5, Trumbull et al., 1996). The temperatures of the final ice melting ($Tm_{ice}$) for the V–L-type fluid inclusions from the Western and Eastern mining areas range from −1.3 to −11.6 °C and −0.8 to −10.3 °C, respectively, and the corresponding salinities are 2.1–15.6 wt.% NaCl equiv. and 1.3–14.3 wt.% NaCl equiv., respectively. Melting temperatures for the $CO_2$ clathrate ($Tm_{clath}$) range from 6.3 to 8.7 °C and the salinities of carbonic fluid inclusions based on the $Tm_{clath}$ are 2.9–9.0 wt.% NaCl equiv. Furthermore, the partial homogenization temperatures of carbonic phase ($Th_{CO_2}$, 15 to 30.1 °C, mostly between 25.8 and 30.1 °C) indicate $CO_2$ densities of ~0.5 g/cm³ (Li et al., 2004a; Trumbull et al., 1996). Daughter mineral-bearing fluid inclusions are too rare and small to carry out reliable microthermometric measurements.

The total homogenization temperatures ($Th_{total}$) for the V-type fluid inclusions captured in the earlier stage range from 336 to 358 °C (Li et al., 2004a), whereas those for the V–L-type inclusions captured in the middle (main mineralization) stage are between 180 and 358 °C (mostly between 245 and 358 °C), which are comparable to those reported by previous studies (Trumbull et al., 1996).

It is worth noting that the average $Th_{total}$ of 322 °C for the Eastern veins is higher than the temperature of 287 °C determined for the Western veins (Fig. 9a). This may indicate that the Eastern veins are closer to the hydrothermal centre. Furthermore, the assemblages of two-phase liquid-rich and vapour-rich fluid inclusions have similar $Th_{total}$, but they have opposite homogenization behaviour. This indicates that the ore fluid immiscibility occurred at the Anjiayingzi deposit (Li et al., 2004a; Trumbull et al., 1996), and such a fluid immiscibility may result in a wide range of salinities in the inclusions (1.3–15.6 wt.% NaCl equiv.) and the local formation of saline-rich fluid inclusions. Such fluid inclusions are common in orogenic gold systems elsewhere (Goldfarb et al., 2005). Trapping pressures estimated from the $CO_2$–$H_2O$ inclusions are 50–110 MPa, corresponding to a depth of ~2 and 4 km under a lithostatic load, or between ~5 and 11 km under a hydrostatic load (Table 5).

From the data presented above, we suggest that the gold veins at Anjiayingzi were deposited at intermediate temperatures between 245 and 358 °C from a $H_2O$–$CO_2$–NaCl fluid system with low–moderate salinities of 1.3–15.6 wt.% NaCl equiv. This mineralizing fluid shares many similarities with typical orogenic gold systems although with relatively higher salinities (mostly <12 wt.% NaCl equiv. for the orogenic gold deposit, Fig. 9b; Goldfarb et al., 2005; Wilkinson, 2001).

### 5.4. H, O, S and Pb isotope geochemistry

Previous researches have produced data on the H, O, S and Pb isotope geochemistry of the Anjiayingzi gold mineralization. These data are tabulated in Appendix A, and have been here recalculated and summarized systematically in Figs. 10–12.

Oxygen and hydrogen of fluid inclusion in quartz from ores have δD values of −80.3 to −96.5‰ and $\delta^{18}O_{H_2O}$ values of 3.7 to 5.5‰, which are interpreted as representing the mineralizing fluid at Anjiayingzi. The fluid inclusion in quartz from the Jiguanzi Quartz Monzonite has δD values of −80.0 to −80.9‰ and $\delta^{18}O_{H_2O}$ values of 8.2 to 9.0‰ (Li et al., 2004a; Zheng et al., 1995). The oxygen and hydrogen stable-isotope values for the fluid from ores and monzonite plot in the bottom left side of typical magmatic and metamorphic fluid fields in Fig. 10, and the values are similar to those from most vein gold deposits worldwide (Chen et al., 2012; Ridley and Diamond, 2000).

The $\delta^{34}S$ values for pyrite from the Western veins are −0.5–1.1‰ and from the Eastern veins are 0.6–5.3‰ (Li, 2000). In addition, the $\delta^{34}S$ values for sulphides from the Western veins average 0.3‰ and are obviously lower than 2.4‰ for those from the Eastern veins (Fig. 11).

The Pb isotope ratios for galena and pyrite from ore at Anjiayingzi are relatively homogeneous with $(^{206}Pb/^{204}Pb)_i$ = 17.088–17.591, $(^{207}Pb/^{204}Pb)_i$ = 15.367–15.578 and $(^{208}Pb/^{204}Pb)_i$ = 37.167–38.091 (Liu, 1992; Wang, 1993; Wang et al., 1994; Zheng et al., 1995). These values generally overlap with the Pb isotope compositions of K-feldspar from the Jiguanzi Quartz Monzonite, with $(^{206}Pb/^{204}Pb)_i$ = 17.194–17.288, $(^{207}Pb/^{204}Pb)_i$ = 15.340–15.391, and $(^{208}Pb/^{204}Pb)_i$ = 37.243–37.392 (Fig. 12; Liu, 1992; Wang, 1993; Wang et al., 1994). The corrected Pb isotope compositions for the metamorphic basement are highly variable, with $(^{206}Pb/^{204}Pb)_i$ = 17.329–17.995, $(^{207}Pb/^{204}Pb)_i$ = 15.585–15.655, and $(^{208}Pb/^{204}Pb)_i$ = 37.574–38.571 (Liu, 1992).

**Table 4**
Results of geothermobarometry for the Jiguanzi Quartz Monzonite.

| Sample spot | JY7-1-13 | JY7-1-14 | JY7-1-15 | JY7-1-16 | JY7-2-14 | JY7-2-15 | JY7-2-16 | JY7-2-17 | JY1-1-9 | JY1-1-10 | JY1-1-11 |
|---|---|---|---|---|---|---|---|---|---|---|---|
| Ab | 81.8 | 75.7 | 77.5 | 79.6 | 81.9 | 81.6 | 79.9 | 79.2 | 77.7 | 72.4 | 73.3 |
| Al (total) | 0.659 | 0.600 | 0.610 | 0.651 | 0.648 | 0.680 | 0.672 | 0.697 | 0.681 | 0.655 | 0.712 |
| $T_{ed-tr}$ (°C) | 736 | 697 | 695 | 716 | 742 | 727 | 730 | 741 | 691 | 719 | 759 |
| $T_{ed-ri}$ (°C) | 648 | 641 | 646 | 662 | 654 | 667 | 662 | 648 | 640 | 652 | 691 |
| $P_{Sch}$ (MPa) | 234 | 248 | 249 | 253 | 258 | 251 | 239 | 156 | 209 | 233 | 253 |
| $P_{AS}$ (MPa) | 248 | 265 | 265 | 261 | 271 | 257 | 248 | 167 | 225 | 245 | 240 |
| Depth (km) | 8.7 | 9.3 | 9.3 | 9.2 | 9.5 | 9.0 | 8.7 | 5.9 | 7.9 | 8.6 | 8.5 |
| $Dep_{aver}$ (km) | | | | | 8.6 | | | | | | |

Ab — the atomic ratio (Na/(Na + Ca + K)) of plagioclase from Table 3; Al (total) — the total number of aluminium cations calculated in the structural formula of hornblende from Table 2; $T_{ed-tr}$ and $T_{ed-ri}$ denote temperatures calculated using plagioclase–hornblende geothermometer A (edenite–tremolite) and geothermometer B (edenite–richterite) of Holland and Blundy (1994), respectively; $P_{Sch}$ — pressure calculated using the barometer of Schmidt (1992); $P_{AS}$ — pressure calculated using $T_{ed-ri}$ and the barometer of Anderson and Smith (1995); depth — emplacement depth according to $P_{AS}$; $Dep_{aver}$ — average emplacement depth of the Jiguanzi Quartz Monzonite.
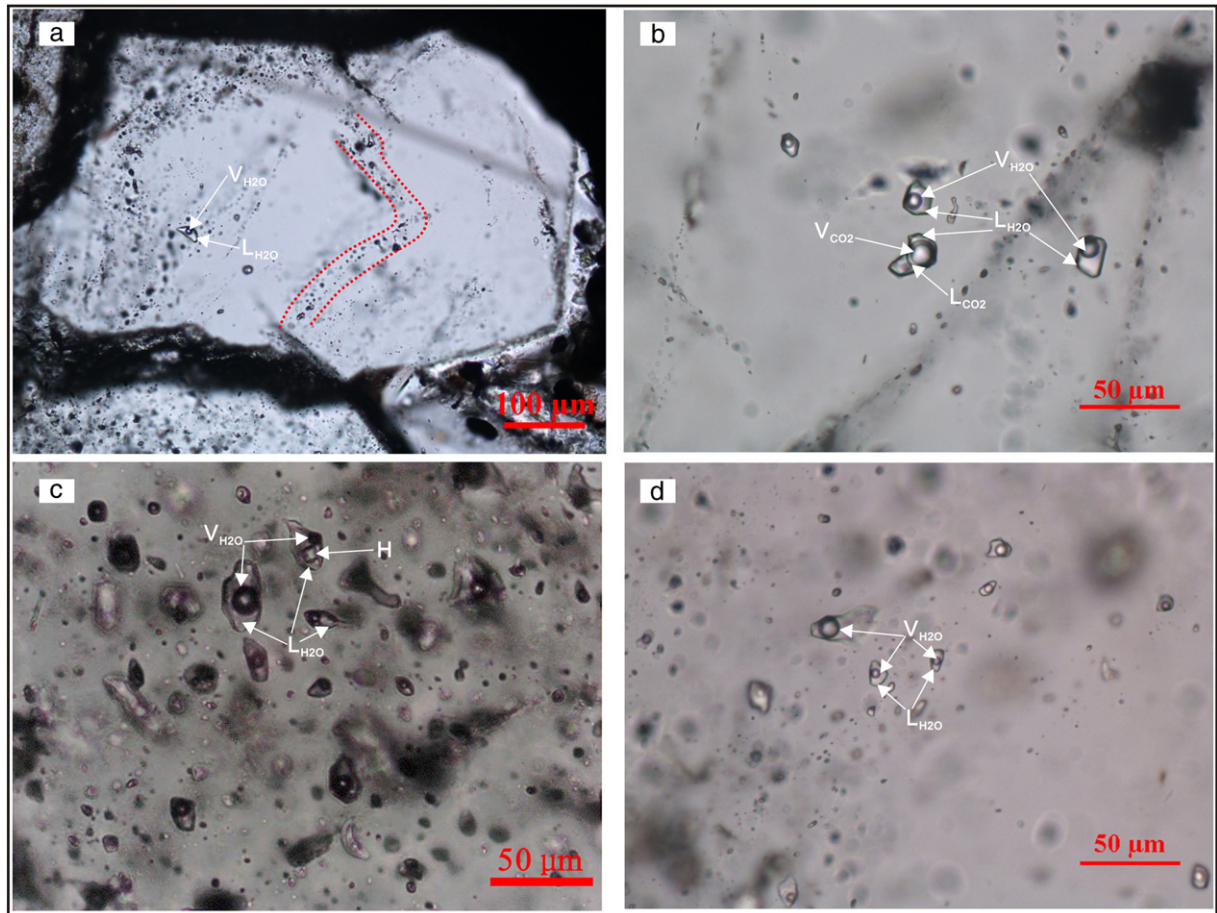
**Fig. 8.** Fluid inclusion types in quartz from the Anjiayingzi gold deposit showing: (a) numerous trails of primary fluid inclusions from a quartz crystal; (b) a cluster of three-phase carbonic and two-phase liquid-rich inclusions; (c) an assemblage of two-phase liquid-rich inclusions and polyphasic inclusions with halite daughter mineral; and (d) isolated two-phase liquid-rich inclusions. Abbreviations: $V_{H_2O}$ — vapour $H_2O$, $L_{H_2O}$ — liquid $H_2O$, $V_{CO_2}$ — vapour $CO_2$, $L_{CO_2}$ — liquid $CO_2$, H — halite.

# 6. Discussion

Although most gold deposits from the NCC are spatially and temporally related to the intrusions and MCCs, their genetic relationship is still not definitive, and this scarcity further prevents us from understanding the gold mineralization process. In this section, we firstly decipher the relationships between MCC exhumation, magma cooling and gold mineralization using the thermochronometric and temperature–pressure–depth data; and then investigate the nature of the Anjiayingzi gold mineralization using evidence from the deposit geology and ore fluid geochemistry. It is acknowledged that although the hypotheses present here may be relevant to the Anjiayingzi deposit, the other deposits in the NCC undoubtedly have complex geological histories which may have involved multiple episodes of gold mineralization or remobilisation (e.g. Song et al., 2016).

## 6.1. Rapid MCC exhumation, magma cooling and gold mineralization

The first recorded motion of the ductile shear of the Kalaqin MCC was initiated at epidote–amphibolite facies conditions at temperatures of ~450–550 °C and a pressure of ~540 MPa corresponding to a depth of between 18 and 20 km (Wang et al., 2011 and references therein). High-quality Ar–Ar and Rb–Sr isochron ages for K-feldspar, biotite and hornblende indicate that the ductile–brittle top-to-the-NE shear deformations took place between ca. 135 and 125 Ma (Liu et al., 2003; Wang and Zheng, 2005; Zhang et al., 2002). K–Ar dating of chlorite indicates that the top-to-the-SE brittle detachment normal faults developed subsequently at ca. 121 Ma (Wang et al., 2006). These data totally indicate that the Kalaqin MCC was cooled and exhumed rapidly from the closure temperature of argon diffusion in hornblende (ca. 600 °C at 135 Ma) to that of K–Ar diffusion in chlorite (ca. 180 °C at 121 Ma) with high rate of

**Table 5**
Microthermometric summary of fluid inclusions in quartz from the Anjiayingzi gold deposit.

| Metallogenic stage | Type | $Tm_{CO_2}$ | $Tm_{ice}$ | $Tm_{clath}$ | $Th_{CO_2}$ | $Th_{total}$ | Salinity | P | Reference |
|---|---|---|---|---|---|---|---|---|---|
| Early | V | | | | | 336–358 | | | Li et al. (2004a) |
| Middle | C | | | 15.0–29.2 | 304–339 | 2.9–6.2 | 50–75 | Li et al. (2004a) |
| Middle | V–L | | | | | 245–290 | 4.0–5.7 | | Li et al. (2004a) |
| Unknown | Primary inclusions | −60.4 to −56.6 | | 6.3–8.7 | 25.8–30.1 | 270–330 | 6.5–9.0 | 50–110 | Trumbull et al. (1996) |
| Middle | V–L from Western lodes | | −1.3 to −11.6 | | | 180–358 | 2.1–15.6 | | This paper |
| Middle | V–L from Western lodes | | −0.8 to −10.3 | | | 258–352 | 1.3–14.3 | | This paper |

Temperatures (T), salinity and pressure (P) are expressed in °C, wt.% NaCl equiv. and MPa, respectively. $Tm_{CO_2}$ — melting temperature of the carbonic phase, $Tm_{ice}$ — temperature of final ice melting, $Tm_{clath}$ — melting temperature of the $CO_2$ clathrate, $Th_{CO_2}$ — partial homogenization temperature of carbonic inclusion, $Th_{total}$ — temperature of total homogenization, V — two-phase vapour-rich fluid inclusions, C — three-phase carbonic fluid inclusions, V–L — two-phase liquid-rich fluid inclusions.
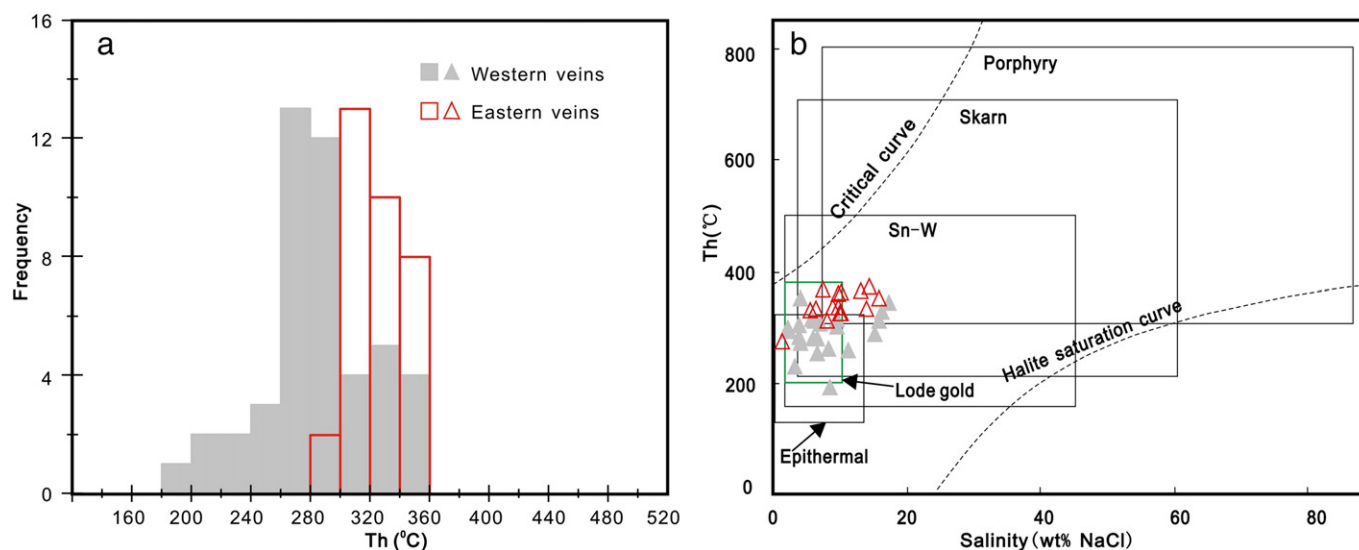
**Fig. 9.** Histograms (a) showing homogenization temperatures of two-phase liquid-rich fluid inclusions, and (b) of homogenization temperatures versus salinities diagram. After Wilkinson (2001).

ca. 30 °C/Ma (Fig. 13). In combination with the complete ductile–brittle deformed rocks developed in the detachment faults, it can be inferred that rapid cooling and exhumation of the Kalaqin MCC are coeval with the structural transition from deep ductile through ductile–brittle to brittle deformation. The cooling rate and exhumation process of the Kalaqin MCC are nearly the same as the Liaonan MCC in the NCC (Fig. 13; Liu et al., 2013), and the Naxos MCC in the Aegean Sea, Greece (Whitney et al., 2013).

When the lithospheric extension is concentrated in a narrow region, the brittle upper crust breaks and is displaced along normal faults and the ductile material ascends from deeper levels of the lithosphere. These processes commonly result in the development of MCC and associated magmatism (Whitney et al., 2013). A typical example is the Early Cretaceous Jiguanzi Quartz Monzonite, which is developed in the footwall of the Kalaqin MCC. As discussed earlier, the weighted mean $^{206}Pb/^{238}U$ age for the monzonite is ca. 133 Ma, which is slightly younger, but within error of the earliest ductile deformation in the Kalaqin

MCC at ca. 135 Ma (Wang and Zheng, 2005). The calculated average pressure of 245 MPa and depth of 8.6 km for the Jiguanzi Quartz Monzonite are lower than those of the initial ductile deformation for the Kalaqin MCC formed at a pressure of ~540 MPa and a depth of ~18–20 km (see above). Thus, the monzonite was emplaced into the MCC during its rapid exhumation. The large variations of monzonite emplacement depths of between 5.9 and 9.5 km further indicate that it ascended in an alternating supra-hydrostatic (ca. 5–16 km) to hydrostatic (ca. 0–5 km) pressure regime (Sibson, 1994), and the emplacement process was also coherent with the structural ductile–brittle transition. The higher crystallization temperatures for the monzonite (ca. 640–691 °C) relative to that of the initial ductile deformation for the Kalaqin MCC (ca. 450–550 °C) indicate that the extensional event forming the MCC was further accentuated by the thermal weakening of the crust. These processes could also result in the rotation of the principal stresses and lead to structural slip along low-angle normal faults (Whitney et al., 2013), both of which are observed in the Kalaqin MCC (Wang and Zheng, 2005; Wang et al., 2004, 2006).
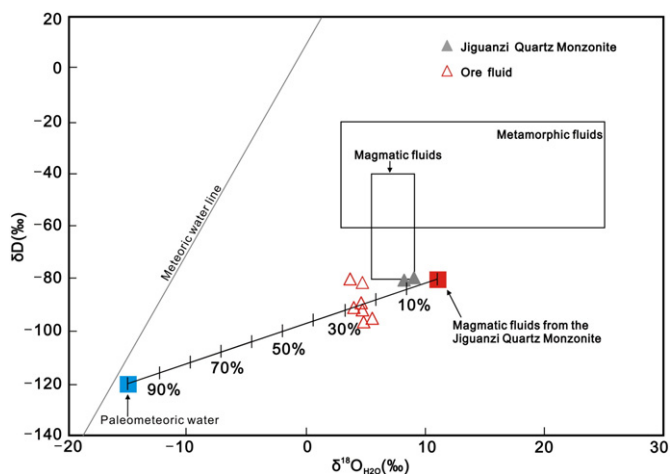


**Fig. 10.** The $\delta D$–$\delta^{18}O_{H_2O}$ plots for mineralizing fluids from the Anjiayingzi gold deposit (after Taylor, 1974). Data are given in Appendix A. The black solid lines with short vertical lines refer to the mixed fluid composition between paleometeoric water ($\delta D = -120‰$, $\delta^{18}O = -15‰$) and magmatic water from the Jiguanzi Quartz Monzonite ($\delta D = -80‰$, $\delta^{18}O = 11‰$). The number (with 10% increments) denotes the proportions of paleometeoric water.
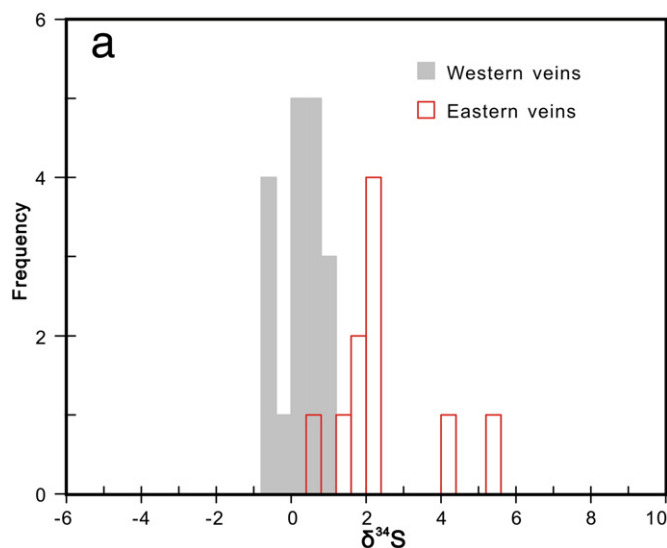


**Fig. 11.** The sulphur isotope compositions of gold-related sulphide minerals from the Anjiayingzi gold deposit. Data are given in Appendix A.
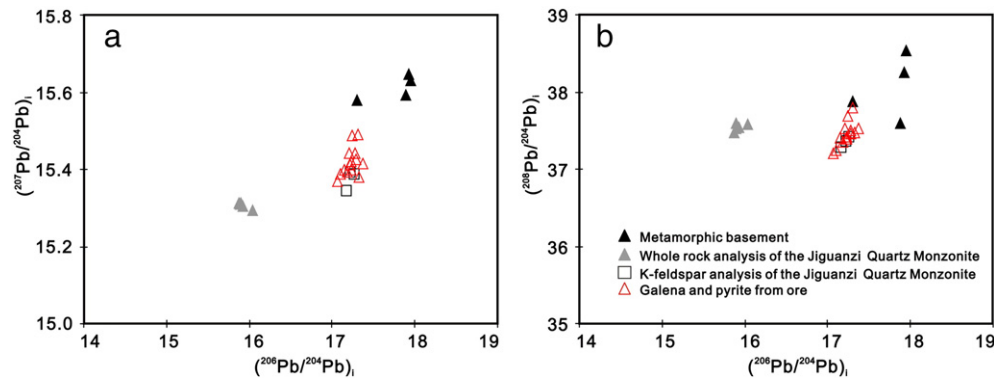
**Fig. 12.** Lead isotope compositions of the Anjiayingzi gold deposit and related lithologies. Data are given in Appendix A.

Zircon U–Pb dating of the Jiguanzi Quartz Monzonite and rhyolite dykes yield ages of ca. 133 Ma (Fig. 6) and ca. 126 Ma (Li et al., 2004b), respectively. Moreover, Rb–Sr ages for biotite from the monzonite range from ca. 130 ± 2 to 126 ± 2 Ma, and eight whole-rock samples from the rhyolite dykes define an isochron age of ca. 122 ± 2 Ma (Trumbull et al., 1996). As shown in Fig. 13, these dates indicate that the monzonite and rhyolite dykes were emplaced during rapid exhumation of the Kalaqin MCC as it underwent rapid cooling from 800 °C (the closure temperature of U–Pb diffusion in zircon) to 300 °C (the closure temperature of Rb–Sr diffusion in biotite). The cooling rate for the monzonite is therefore estimated to be ~71 °C/Ma, or ~42 °C/Ma if we accept the ca. 138 Ma age for the monzonite, which is higher than that of 30 °C/Ma for the Kalaqin MCC. The high cooling rate for the monzonite is also a feature of intrusions in the Liaonan MCC (Liu et al., 2013), and that of Guojialing Granite in the Linglong MCC on the Jiaodong Peninsula (Fig. 13; Charles et al., 2013).

Field investigation shows that some rhyolite dykes hosted by the Jiguanzi Quartz Monzonite cross-cut gold veins that are also locally enriched in pyrite (Li et al., 2004b). These geological observations indicate that the gold mineralization at Anjiayingzi is late relative to the emplacement of host pluton, and is coeval with or slightly earlier than

the formation of rhyolite dykes. We therefore believe that the zircon U–Pb data for the monzonite and rhyolite dykes described above indicate that the Anjiayingzi gold deposit was formed between ca. 133 and 126 Ma during rapid cooling of the host monzonite. The timing of the gold mineralization at Anjiayingzi is nearly the same as that of eastern Jinchanggouliang in the Nulu'erhu Uplift where there is a molybdenite Re–Os age of ca. 131 Ma (Hou, 2011) and that of Paishanlou in the Yiwulüshan MCC where there is a biotite Ar–Ar age of ca. 127 Ma (Zhang et al., 2005).

Based on the spatial and temporal relationships discussed above, it is concluded that the Anjiayingzi gold deposit was formed during rapid cooling of the Jiguanzi Quartz Monzonite and the fast exhumation and cooling of the Kalaqin MCC (Fig. 13). In addition, the change of ore-bearing structures, from the Eastern ductile–brittle to the Western brittle faults, may also record the continuous exhumation of the Kalaqin MCC from the ductile to brittle regimes. During MCC exhumation and the structural transition, ore-controlling faults evolved from a supra-hydrostatic regime at a depth of 5–16 km to a hydrostatic regime at a depth of <5 km (Sibson, 1994). The estimated average depositional temperatures of 245–358 °C, trapping pressures of 250–110 MPa, and a depth of 2.5–7.5 km for the mineralising fluids thus correspond to the alternating supra-hydrostatic to hydrostatic pressure conditions. Furthermore, fluid immiscibility of the Anjiayingzi gold deposit may be another significant product of pressure fluctuations, as observed in typical orogenic gold systems (Goldfarb et al., 2005).

The formation mechanism of the Anjiayingzi gold mineralization may be applicable to other polymetallic ore deposits such as the Tethyan Eurasian and North American Cordillera metallogenic belts (e.g. Whitney et al., 2013 and reference therein). In the Muteh gold deposit from the Sanandaj–Sirjam zone located in the Zagros Orogen in Iran, both ductile fabrics and gold ore-controlling structures are interpreted to have been formed within a single, continuous extensional event (Moritz et al., 2006). This event started with ductile deformation and gradually evolved into brittle deformation. Radiometric age data indicate that gold deposition at Muteh occurred during or after the late stages of the extensional event that was associated with the exhumation of the host metamorphic complex, and coeval with regional magmatism in the Sanandaj–Sirjam Zone (Moritz et al., 2006). The model may also apply in the Alpine tectonic terranes of the Central Rhodopian MCC in Bulgaria and Greece, Bjala Reka MCC in Bulgaria, and the Kesebir–Kardamos Dome in Bulgaria and Greece (Rohrmeier et al., 2013). Polymetallic Cu–Au–Ag–Pb–Zn mineralization, volcanism and extension of the high-grade basement in these areas overlap within a ~5 Ma time interval during rapid cooling and exhumation of the footwall (Bonev et al., 2013; Rohrmeier et al., 2013). The estimated cooling rate of 30 °C/Ma for the Kalaqin MCC is also comparable to the estimated rate of 35 °C/Ma for the Bjala Reka MCC and Kesebir–Kardamos Dome (Bonev et al., 2013).
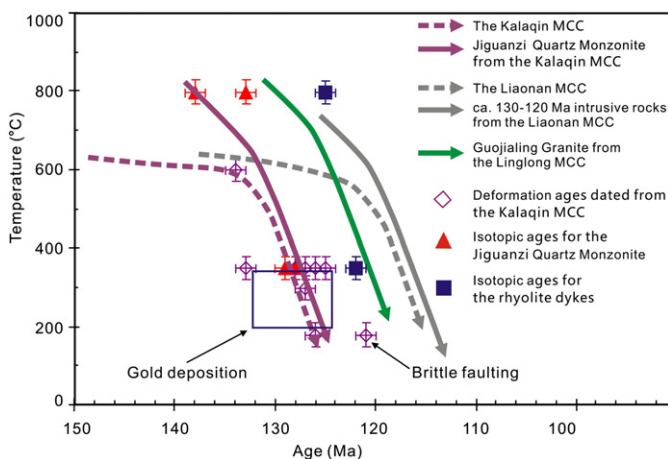


**Fig. 13.** Cooling paths for the Kalaqin MCC and Jiguanzi Quartz Monzonite according to radiometric ages listed on Fig. 2a. The cooling paths of Liaonan MCC and associated intrusion are modified from Liu et al. (2013), and that for Guojialing Granite are from Charles et al. (2013). The T–t conditions for gold deposition are also illustrated. Mean mineral closure temperatures: biotite Rb–Sr — 350 °C, biotite, K-feldspar, plagioclase, and whole rock internal Rb–Sr isochron — 300 °C (Liu et al., 2003); zircon U–Pb — 800 °C, hornblende Ar–Ar — 600 °C, biotite Ar–Ar — 350 °C (Reiners et al., 2005); and K-feldspar and chlorite K–Ar — 180 °C (Wang et al., 2006). The uncertainties for closure temperatures and ages are 30 °C and 1 Ma, respectively.

## 6.2. Relationship between the Anjiayingzi gold mineralization and magmatism

The present understanding of the Early Cretaceous vein gold deposits around the NCC place them in a category of orogenic gold deposits, based on the combination of geological characteristics, mineralization style, ore and alteration assemblages, and ore fluid compositions (Chen et al., 2004; Goldfarb et al., 2001, 2007, 2014; Hart et al., 2002; Jiang et al., 2009; Mao et al., 2002; Zhou and Goldfarb, 2002). We have shown a number of features which make it difficult to classify the Anjiayingzi gold deposit as a product of orogenesis. Firstly, the ca. 135–121 Ma timing of the mineralization overlaps with the development and evolution of the Kalaqin MCC. MCCs have been recognized in continental settings, at spreading mid-ocean ridges, and in continental rifts. In each of these tectonic settings, MCCs are essentially important rheologic pattern of extension, and the extension is the driving force for their exhumation. During extension, heat, fluid and ore material are transferred from deep, hot and ductile zones to shallow, cool and brittle levels, and economically important mineral deposits are formed during this process (Whitney et al., 2013). Consequently, the coeval occurrence of the Anjiayingzi gold veins and Kalaqin MCC indicates that this gold mineralization formed in a regional extensional setting. This conclusion is also supported by the contemporaneous occurrences of regional rift-basins and intense crustal–mantle derived magmatism found in the NCC (Meng, 2003; Yang et al., 2008; Zhu et al., 2012). The Early Cretaceous basins in the craton are fault-controlled, and more than 100 km of horizontal lithospheric stretching is possible (Meng, 2003; Ren et al., 2002; Zhu et al., 2012). Moreover, magmatism characterised by alkaline syenite–granite–rhyolite suites in the northern NCC peaked between ca. 130 and 120 Ma, which also indicates an extensional tectonic setting (Yang et al., 2008). The extensional geodynamic setting for the Anjiayingzi gold deposit is therefore different when compared to classic orogenic gold deposits formed in a compressional and transpressional setting during the late stages of accretion or collision orogeny (Goldfarb et al., 2014; Groves et al., 2003).

We also show that there is a >2 billion year time gap between the Early Cretaceous monzonite host for the Anjiayingzi gold deposit and Neoarchean to Early Palaeoproterozoic (ca. 2485–2401 Ma) metamorphism of the monzonite's host Jianping Group (Liu et al., 2011). This rules out an Early Paleoproterozoic metamorphic-devolatilization as a source for ore fluids and metals for the Early Cretaceous monzonite-hosted Anjiayingzi deposit, and so they cannot be classified as an orogenic gold deposit sensu-stricto (Goldfarb and Santosh, 2014; Zhou et al., 2014). The large time gap between the gold mineralization and early regional metamorphism is also observed in the Jiaodong and Xiaoqinling gold fields which are part of the Early Cretaceous large-scale gold mineralization around NCC (Goldfarb and Santosh, 2014; Li et al., 2012a, 2012b).

The low Au/Ag ratios of <1, low gold fineness (700–850), and high sulphide content (4–30 vol.%) for the Anjiayingzi deposit are different when compared to those of typical orogenic gold deposits, which have values of 5–10, >900 and 2–5 vol.%, respectively (Goldfarb et al., 2005).

The He, Ar and C isotope compositions of the ore fluids from Early Cretaceous gold deposits along the northern NCC indicate a significant mantle fluid contribution for major vein gold deposits (Li and Santosh, 2014), which is also different when compared to classic orogenic gold deposits where the ore fluids are derived from metamorphism (Goldfarb et al., 2005).

The $\delta D$ value of $-80.3$ to $-96.5‰$ and the $\delta^{18}O_{H_2O}$ value of 3.7–5.5‰ for the ore fluids, and the $\delta D$ value of $-80.0$ to $-80.9‰$ and the $\delta^{18}O_{H_2O}$ value of 8.2–9.0‰ for the Jiguanzi Quartz Monzonite plot in the bottom left-hand corner of the typical magmatic and metamorphic fluid fields in Fig. 10. This plot alone, therefore, cannot provide clear constraints on the source of the mineralizing fluids. Whereas, the mixing trend between the fluids derived from the host intrusion and the inferred paleometeoric water can explain the composition of the ore fluids. The curve closely approaches the compositions of ore fluids with a contribution of 20–30% paleometeoric water (Fig. 10). The magmatic and subordinate paleometeoric fluids may be the main source for the ore-forming fluids. It is common that meteoric fluids infiltrate detachment faults and penetrated into the uppermost levels of an intrusion during the late stage of extension, and both of magmatic and paleometeoric fluids can play key roles in the formation of polymetallic mineralization (e.g. Eliopoulos and Kilias, 2011; Hetzel et al., 2013; Holk and Taylor, 2007; Siebenaller et al., 2013). However, veinlet and sheeted networks would be produced when fluids exsolved from the roof zones of intrusions (Goldfarb and Santosh, 2014), which is not the case for the Anjiayingzi gold deposit. Therefore, we suggest that a magma chamber near the eastern master detachment fault was present at depth beneath the fault. This conjecture is supported by the occurrences of a number of later mafic magmatic enclaves hosted by the monzonite (Fu et al., 2012b). The abundant late rhyolite dykes present in the eastern part of the Loufengmao–Nandawa district further indicate that the hydrothermal centre is in this area (Fig. 3b).

The higher average $\delta^{34}S$ value of 2.4‰ and Th$_{total}$ value of 322 °C for the Eastern veins than those from the Western veins (0.3‰ and 287 °C), which are similar to the Victory–Defiance gold deposits in the Eastern Goldfields Superterrane of Western Australia (Hodkiewicz et al., 2009), may provide more evidence about movement and heat transfer in the ore fluids. The physicochemical parameters of ore fluids, including the temperature, isotope composition of sulphur, $f_{O_2}$ and pH values, can influence the isotope composition of hydrothermal sulphides (Ohmoto, 1972). A theoretical negative correlation between temperature and $\delta^{34}S$ for pyrite indicates that the differences in $\delta^{34}S$ between the Eastern and Western veins are not caused by temperature alone (Ohmoto, 1972). The similar mineral assemblages and consistent pH values of 4.8–5.1 (Zheng et al., 1995) for the Eastern and Western veins also indicate that the sulphur isotope composition and pH of the ore fluids is not the key controlling factor responsible for the differences. Consequently, we propose that differences in $\delta^{34}S$ between pyrite from the Eastern and Western are controlled by $f_{O_2}$ of the ore fluids. The Eastern veins are hosted by brittle–ductile faults and the Western veins are hosted by brittle faults. These geological features indicate that the Western veins were formed relatively late under brittle conditions, whereas the Eastern veins were formed earlier under brittle–ductile conditions. The Western veins are more dilational and the corresponding ore fluids are more oxidised, which would result the lower $\delta^{34}S$ of pyrite. Gradual changes from the earlier high-temperature and relatively reduced mineralised fluids for the Eastern veins to the later low-temperature and relatively oxidised ore fluids for Western veins, may further indicate that these fluids were transferred from east to west, and the hydrothermal centre and concealed intrusion are near the eastern Louzidian detachment fault in the Kalaqin MCC.

Moreover, the consistent Pb isotope compositions of ore sulphides and K-feldspar from the Jiguanzi Quartz Monzonite indicate that the metals at the Anjiayingzi gold deposit may also derived from the eastern concealed intrusion (Fig. 12). Therefore, we suggest that the ore fluids, sulphur and metals at Anjiayingzi were related directly or indirectly to the degassing and devolatilization of an Early Cretaceous magma chamber near the eastern master detachment fault. Fluid immiscibility and mixing with paleometeoric water, accompanied by the structural transition and resultant fluid pressure fluctuations, may have caused the rapid precipitation of sulphides carrying Au. Gold deposition took place during rapid cooling of the Jiguanzi Quartz Monzonite and fast exhumation and cooling of the Kalaqin MCC.

The occurrences of the Anjiayingzi gold mineralization, Jiguanzi Quartz Monzonite, Kalaqin MCC, and regional rift-basins around the NCC are subsurface responses to lithospheric destruction during the Early Cretaceous. These geological events may have been triggered by the westward subduction of the Paleo-Pacific/Izanagi slab (Goldfarb and Santosh, 2014; Li and Santosh, 2014; Li et al., 2012a; Mao et al., 2008; Tan et al., 2012; Yang et al., 2003; Zhai and Santosh, 2013).

## 7. Conclusions

1. A two-stage extension is recognized from the Kalaqin MCC. The first is recorded in the top-to-the-NE ductile–brittle shear deformation at 135–125 Ma and the second in the top-to-the-NW and SE brittle detachment normal faults beginning at ca. 121 Ma. The initial ductile shearing at the Kalaqin MCC was formed at epidote–amphibolite facies conditions (450–550 °C, 540 MPa) at a depth of 18–20 km.

2. The Jiguanzi Quartz Monzonite was emplaced at ca. 133 Ma with crystallization temperatures of 640–691 °C and pressures of 167–271 MPa. The emplacement of the monzonite took place at a depth of 5.9–9.5 km, indicating that the magma ascended into the Kalaqin MCC during its rapid exhumation, and further strengthened the crustal weakening and MCC extension.

3. The Anjiayingzi gold deposit was formed between ca. 133 and 126 Ma during rapid cooling of the Jiguanzi Quartz Monzonite at a rate of 42–71 °C/Ma, and exhumation and cooling of the Kalaqin MCC at a rate of 30 °C/Ma. Gold mineralization was resulted from fluid immiscibility and mixing along the structural transition from ductile–brittle to brittle deformation, during fluid-pressure fluctuations between supra-hydrostatic and hydrostatic regimes.

4. The extensional setting of the Anjiayingzi gold mineralization and the >2 billion year time gap between the mineralization and regional metamorphism of the basement in the region rule out a metamorphic-devolatilization derivation for the mineralising fluids. Combining the H–O–S–Pb isotope compositions, we suggest that there is a magmatic origin for the intermediate-temperature $H_2O$–$CO_2$–NaCl mineralizing fluids, sulphur and metals.

## Appendix A

**Table A1**
The $\delta D$ (‰), $\delta^{18}O_{H_2O}$ (‰), $\delta^{34}S_{V-CDT}$ (‰) and Pb isotope compositions of the Anjiayingzi gold deposit.

| Sample | Mineral | $\delta D$ | $\delta^{18}O_{H_2O}$ | $\delta^{34}S_{V-CDT}$ | $^{206}Pb/^{204}Pb$ | $^{207}Pb/^{204}Pb$ | $^{208}Pb/^{204}Pb$ | Reference |
|---|---|---|---|---|---|---|---|---|
| D-1 | Quartz of Jiguanzi Quartz Monzonite | −80.0 | 9.0 | | | | | Li et al. (2004a) |
| D-1 | Quartz of Jiguanzi Quartz Monzonite | −80.9 | 8.2 | | | | | Zheng et al. (1995) |
| LSM01 | Quartz from ore | −81.6 | 4.7 | | | | | Li et al. (2004a) |
| LSM02 | Quartz from ore | −96.5 | 4.8 | | | | | Li et al. (2004a) |
| NDW1 | Quartz from ore | −92.2 | 4.7 | | | | | Li et al. (2004a) |
| SQ3107 | Quartz from ore | −80.3 | 3.7 | | | | | Zheng et al. (1995) |
| SQ2-2 | Quartz from ore | −95.1 | 5.5 | | | | | Zheng et al. (1995) |
| NDW | Quartz from ore | −89.6 | 4.6 | | | | | Zheng et al. (1995) |
| 91EW-4 | Quartz from ore | −91.0 | 4.0 | | | | | Zheng et al. (1995) |
| YP1-2-42 | Pyrite from Western lodes | | | 0.2 | | | | Li (2000) |
| YP2-3-41 | Pyrite from Western lodes | | | 0.6 | | | | Li (2000) |
| YP2-5-29 | Pyrite from Western lodes | | | −0.3 | | | | Li (2000) |
| YP2-5-31 | Pyrite from Western lodes | | | 0.6 | | | | Li (2000) |
| YP3-6-19 | Pyrite from Western lodes | | | 0.5 | | | | Li (2000) |
| YP3-6-23 | Pyrite from Western lodes | | | 0.4 | | | | Li (2000) |
| YP3-7-09 | Pyrite from Western lodes | | | 0.3 | | | | Li (2000) |
| YP4-6-13 | Pyrite from Western lodes | | | 0.3 | | | | Li (2000) |
| YP4-5-27 | Pyrite from Western lodes | | | 1.1 | | | | Li (2000) |
| YP4-6-15 | Pyrite from Western lodes | | | 0.5 | | | | Li (2000) |
| YP4-7-03 | Pyrite from Western lodes | | | 0.8 | | | | Li (2000) |
| GB3-0-30 | Pyrite from Western lodes | | | 0.8 | | | | Li (2000) |
| GB3-1-19 | Pyrite from Western lodes | | | 0.3 | | | | Li (2000) |
| GB3-1-25 | Pyrite from Western lodes | | | −0.4 | | | | Li (2000) |
| GB3-2-15 | Pyrite from Western lodes | | | 0.2 | | | | Li (2000) |
| GB3-3-04 | Pyrite from Western lodes | | | −0.4 | | | | Li (2000) |
| GB3-3-08 | Pyrite from Western lodes | | | −0.4 | | | | Li (2000) |
| GB3-4-01 | Pyrite from Western lodes | | | −0.5 | | | | Li (2000) |
| D1-2-06 | Pyrite from Eastern lodes | | | 1.4 | | | | Li (2000) |
| D1-2-09 | Pyrite from Eastern lodes | | | 0.6 | | | | Li (2000) |
| D1-3-11 | Pyrite from Eastern lodes | | | 2.0 | | | | Li (2000) |
| D1-3-13 | Pyrite from Eastern lodes | | | 2.1 | | | | Li (2000) |
| D1-4-17 | Pyrite from Eastern lodes | | | 2.3 | | | | Li (2000) |
| LT6-1-04 | Pyrite from Eastern lodes | | | 5.3 | | | | Li (2000) |
| LT6-2-02 | Pyrite from Eastern lodes | | | 2.0 | | | | Li (2000) |
| LTS-07 | Pyrite from Eastern lodes | | | 2.3 | | | | Li (2000) |
| LT8-1-11 | Pyrite from Eastern lodes | | | 4.2 | | | | Li (2000) |
| LA8-1-13 | Pyrite from Eastern lodes | | | 1.7 | | | | Li (2000) |
| M-3 | whole rocks of Jianping Group | | | | 17.930 | 15.599 | 37.574 | Liu (1992) |
| T-2 | whole rocks of Jianping Group | | | | 17.329 | 15.585 | 37.881 | Liu (1992) |
| T-3 | whole rocks of Jianping Group | | | | 17.977 | 15.655 | 38.271 | Liu (1992) |
| T-4 | whole rocks of Jianping Group | | | | 17.995 | 15.638 | 38.571 | Liu (1992) |
| g-9 | K-feldspar of Jiguanzi Quartz Monzonite | | | | 17.288 | 15.386 | 37.392 | Wang et al. (1994) |
| 9-10 | K-feldspar of Jiguanzi Quartz Monzonite | | | | 17.194 | 15.340 | 37.243 | Wang (1993) |
| 9-11 | K-feldspar of Jiguanzi Quartz Monzonite | | | | 17.250 | 15.391 | 37.341 | Liu (1992) |

**Table A1** (continued)

| Sample | Mineral | $\delta D$ | $\delta^{18}O_{H_2O}$ | $\delta^{34}S_{V-CDT}$ | $^{206}Pb/^{204}Pb$ | $^{207}Pb/^{204}Pb$ | $^{208}Pb/^{204}Pb$ | Reference |
|---|---|---|---|---|---|---|---|---|
| LFM-2 | Galena | | | | 17.354 | 15.379 | 37.455 | Zheng et al. (1995) |
| 9-1 | Galena | | | | 17.591 | 15.578 | 38.091 | Wang (1993) |
| 9-2 | Galena | | | | 17.176 | 15.397 | 37.379 | Wang (1993) |
| 9-3 | Galena | | | | 17.236 | 15.443 | 37.507 | Wang (1993) |
| 9-4 | Galena | | | | 17.338 | 15.492 | 37.793 | Wang (1993) |
| 9-5 | Galena | | | | 17.269 | 15.489 | 37.681 | Wang (1993) |
| 9-6 | Galena | | | | 17.306 | 15.441 | 37.438 | Liu (1992) |
| AK-2 | Galena | | | | 17.126 | 15.387 | 37.209 | Wang et al. (1994) |
| AK-3 | Galena | | | | 17.259 | 15.419 | 37.396 | Wang et al. (1994) |
| A$_3$-4-1 | Galena | | | | 17.260 | 15.397 | 37.366 | Wang et al. (1994) |
| A$_3$-3-1 | Pyrite | | | | 17.244 | 15.411 | 37.368 | Wang et al. (1994) |
| A$_4$-1-1 | Pyrite | | | | 17.088 | 15.367 | 37.167 | Wang et al. (1994) |
| B$_1$-6-1 | Pyrite | | | | 17.211 | 15.391 | 37.321 | Wang et al. (1994) |
| C$_3$-2-1 | Pyrite | | | | 17.314 | 15.425 | 37.480 | Wang et al. (1994) |
| D$_3$-3-1 | Pyrite | | | | 17.406 | 15.414 | 37.506 | Wang et al. (1994) |

$\delta^{18}O_{H_2O}$ — fluids in equilibrium with quartz using the equation $1000\ln\alpha_{quartz-water} = 3.38 \times 10^6\,T^{-2} - 3.40$ (Clayton et al., 1972), where the temperatures used in calculation are the averages of fluid inclusion homogenization temperatures. $^{206}Pb/^{204}Pb$, $^{207}Pb/^{204}Pb$ and $^{208}Pb/^{204}Pb$ of whole rock are calculated at t = 133 Ma.

# References

Anderson, J.L., Smith, D.R., 1995. The effects of temperature and $f_{O_2}$ on the Al-in-hornblende barometer. Am. Mineral. 80, 549–559.

Anderson, J.L., Barth, A.P., Wooden, J.L., Mazdab, F., 2008. Thermometers and thermobarometers in granitic systems. Rev. Mineral. Geochem. 69, 121–142.

Bonev, N., Spikings, R., Moritz, R., Marchev, P., Collings, D., 2013. $^{40}Ar/^{39}Ar$ age constraints on the timing of Tertiary crustal extension and its temporal relation to ore-forming and magmatic processes in the Eastern Rhodope Massif, Bulgaria. Lithos 180–181, 264–278.

Brown, P.E., Hagemann, S.G., 1995. MacFlinCor and its application to fluids in Archean lode-gold deposits. Geochim. Cosmochim. Acta 59, 3943–3952.

Charles, N., Gumiaux, C., Augier, R., Chen, Y., Zhu, R., Lin, W., 2011. Metamorphic core complexes vs. synkinematic plutons in continental extension setting: Insights from key structures (Shandong Province, eastern China). J. Asian Earth Sci. 40, 261–278.

Charles, N., Augier, R., Gumiaux, C., Monie, P., Chen, Y., Faure, M., Zhu, R.X., 2013. Timing, duration and role of magmatism in wide rift systems: insights from the Jiaodong Peninsula (China, East Asia). Gondwana Res. 24, 412–428.

Chen, Y.J., Pirajno, F., Lai, Y., Li, C., 2004. Metallogenic time and tectonic setting of the Jiaodong gold province. Acta Petrol. Sin. 20, 907–922 (in Chinese with English abstract).

Chen, B., Jahn, B.M., Tian, W., 2009. Evolution of the Solonker suture zone: Constraints from zircon U–Pb ages, Hf isotopic ratios and whole-rock Nd–Sr isotope compositions of subduction- and collision-related magmas and forearc sediments. J. Asian Earth Sci. 34, 245–257.

Chen, H.Y., Chen, Y.J., Baker, M., 2012. Isotopic geochemistry of the Sawayaerdun orogenic-type gold deposit, Tianshan, northwest China: implications for ore genesis and mineral exploration. Chem. Geol. 310–311, 1–11.

Clayton, R.N., O'Neil, J.R., Mayeda, T.K., 1972. Oxygen isotope exchange between quartz and water. J. Geophys. Res. 77, 3057–3067.

Davis, G.A., Zheng, Y.D., 2002. Metamorphic core complexes: definition, types and tectonic setting. Geol. Bull. China 21, 185–192 (in Chinese with English abstract).

Davis, G.A., Wang, C., Zheng, Y.D., Zhang, J.J., Zhang, C.H., Gehrels, G.E., 1998. The enigmatic Yinshan fold-and-thrust belt of northern China: new views on its intraplate contractional styles. Geology 26, 43–46.

Eliopoulos, D.G., Kilias, S.P., 2011. Marble-hosted submicroscopic gold mineralization at Asimotrypes area, Mount Pangeon, Southern Rhodope core complex, Greece. Econ. Geol. 106, 751–780.

Fang, M.L., Tong, H.S., 1995. A tectonic study of Dashuiqing gold orefield in Kalaqin county, Inner Mongolia. Geotecton. Metallog. 19, 178–187 (in Chinese with English abstract).

Fu, L.B., Wei, J.H., Kusky, T.M., Chen, H.Y., Tan, J., Li, Y.J., Kong, L.J., Jiang, Y.J., 2012a. Triassic shoshonitic dykes from the northern North China craton: petrogenesis and geodynamic significance. Geol. Mag. 149, 39–55.

Fu, L.B., Wei, J.H., Kusky, T.M., Chen, H.Y., Tan, J., Li, Y.J., Shi, W.J., Chen, C., Zhao, S.Q., 2012b. The Cretaceous Duimiangou adakite-like intrusion from the Chifeng region, northern North China Craton: crustal contamination of basaltic magma in an intracontinental extensional environment. Lithos 134–135, 273–288.

Goldfarb, R.J., Santosh, M., 2014. The dilemma of the Jiaodong gold deposits: are they unique? Geosci. Front. 5, 139–153.

Goldfarb, R.J., Groves, D.I., Gardoll, S., 2001. Orogenic gold and geologic time: a global synthesis. Ore Geol. Rev. 18, 1–75.

Goldfarb, R.J., Baker, T., Dubé, B., Groves, D.I., Hart, C.J.R., Gosselin, P., 2005. Distribution, character, and genesis of gold deposits in metamorphic terranes. Economic Geology 100th Anniversary Volume, pp. 407–450.

Goldfarb, R.J., Hart, C., Davis, G., Groves, D., 2007. East Asian gold: deciphering the anomaly of Phanerozoic gold in Precambrian cratons. Econ. Geol. 102, 325–341.

Goldfarb, R.J., Taylor, R.D., Collins, G.S., Goryachev, N.A., Orlandini, O.F., 2014. Phanerozoic continental growth and gold metallogeny of Asia. Gondwana Res. 25, 48–102.

Groves, D.I., Goldfarb, R.J., Robert, F., Hart, C.J.R., 2003. Gold deposits in metamorphic belts: overview of current understanding, outstanding problems, future research, and exploration significance. Econ. Geol. 98, 1–29.

Han, B.F., Zheng, Y., Gan, J., Chang, Z., 2001. The Louzidian normal fault near Chifeng, Inner Mongolia: master fault of a quasi-metamorphic core complex. Int. Geol. Rev. 43, 254–264.

Han, G.Q., Liu, Y.J., Neubauer, F., Genser, J., Zou, Y.X., Li, W., Liang, C.Y., 2012. Characteristics, timing, and offsets of the middle-southern segment of the western boundary strike-slip fault of the Songliao Basin in Northeast China. Sci. China Earth Sci. 55, 464–475.

Hart, C.J.R., Goldfarb, R.J., Qiu, Y.M., Snee, L., Miller, L.D., Miller, M.L., 2002. Gold deposits of the northern margin of the North China Craton: multiple late Paleozoic–Mesozoic mineralizing events. Miner. Deposita 37, 326–351.

Hetzel, R., Zwingmann, H., Mulch, A., Gessner, K., Akal, C., Hampel, A., Güngör, T., Petschick, R., Mikes, T., Wedin, F., 2013. Spatiotemporal evolution of brittle normal faulting and fluid infiltration in detachment fault systems: a case study from the Menderes Massif, western Turkey. Tectonics 32, 364–376.

Hodkiewicz, P.F., Groves, D.I., Davidson, G.J., Weinberg, R.F., Hagemann, S.G., 2009. Influence of structural setting on sulphur isotopes in Archean orogenic gold deposits, Eastern Goldfields Province, Yilgarn, Western Australia. Miner. Deposita 44, 129–150.

Holk, G.J., Taylor, H.P., 2007. $^{18}O/^{16}O$ evidence for contrasting hydrothermal regimes involving magmatic and meteoric-hydrothermal waters at the valhalla metamorphic core complex, British Columbia. Econ. Geol. 102, 1063–1078.

Holland, T., Blundy, J., 1994. Non-ideal interactions in calcic amphiboles and their bearing on amphibole–plagioclase thermometry. Contrib. Mineral. Petrol. 116, 433–447.

Hou, W.R., 2011. Contrast study on the Hadamengou gold deposit and Jinchanggouliang gold deposit, Inner Mongolia(Ph.D. Thesis) Chinese Academy of Geological Sciences, Beijing (in Chinese with English abstract).

Jahn, B.M., Auvray, B., Cornichet, J., Bai, Y.L., Shen, Q.H., Liu, D.Y., 1987. 3.5 Ga old amphibolites from eastern Hebei Province, China: field occurrence, petrography, Sm–Nd isochron age and REE geochemistry. Precambrian Res. 34, 311–346.

Jiang, S.Y., Dai, B.Z., Jiang, Y.H., Zhao, H.X., Hou, M.L., 2009. Jiaodong and Xiaoqinling: two orogenic gold provinces formed in different tectonic settings. Acta Petrol. Sin. 25, 2727–2738 (in Chinese with English abstract).

Kusky, T.M., Windley, B.F., Zhai, M.G., 2007. Lithospheric thinning in eastern Asia; constraints, evolution, and tests of models. In: Zhai, M.G., Windley, B.F., Kusky, T.M., Meng, Q.R. (Eds.), Mesozoic Sub-Continental Lithospheric Thinning Under Eastern Asia. Geological Society of London, Special Publication 280, pp. 331–343.

Leake, B.E., Woolley, A.R., Arps, C., Birch, W.D., Gilbert, M.C., Grice, J.D., Hawthorne, F.C., Kato, A., Kisch, H.J., Krivovichev, V.G., Linthout, K., Laird, J., Mandarino, J.A., Maresch, W.V., Nickel, E.H., Rock, N., Schumacher, J.C., Smith, D.C., Stephenson, N., Ungaretti, L., Whittaker, E., Guo, Y.Z., 1997. Nomenclature of amphiboles: report of the subcommittee on amphiboles of the International Mineralogical Association, Commission on New Minerals and Mineral Names. Can. Mineral. 35, 219–246.

Li, Y.G., 2000. Metallogenic regularities and prognosis of Jinchanshan gold deposit, Kalaqin, Inner Mongolia. Unpublished report of Jinchan Mining Ltd. (in Chinese).

Li, S.R., Santosh, M., 2014. Metallogeny and craton destruction: records from the North China Craton. Ore Geol. Rev. 56, 376–414.

Li, Y.G., Zhai, M.G., Miao, L.C., Xue, L.W., Zhu, J.W., Guan, H., 2004a. Ore-forming fluids of the Anjiayingzi gold deposit in Chifeng region, Inner Mongolia. Acta Petrol. Sin. 20, 961–968 (in Chinese with English abstract).

Li, Y.G., Zhai, M.G., Yang, J.H., Miao, L.C., Guan, H., 2004b. Gold mineralization age of the Anjiayingzi gold deposit in Chifeng County, Inner Mongolia and implications for Mesozoic metallogenic explosion in North China. Sci. China Earth Sci. 47, 115–121.

Li, J.B., Wang, T., Ouyang, Z.X., 2010. Strain and kinematic vorticity analysis of the Louzidian low-angle ductile shear detachment zone in Chifeng, Inner Mongolia, China. Sci. China Earth Sci. 53, 1611–1624.

Li, J.W., Bi, S.J., Selby, D., Chen, L., Vasconcelos, P., Thiede, D., Zhou, M.F., Zhao, X.F., Li, Z.K., Qiu, H.N., 2012a. Giant Mesozoic gold provinces related to the destruction of the North China craton. Earth Planet. Sci. Lett. 349–350, 26–37.

Li, J.W., Li, Z.K., Zhou, M.F., Chen, L., Bi, S.J., Deng, X.D., Qiu, H.N., Cohen, B., Selby, D., Zhao, X.F., 2012b. The Early Cretaceous Yangzhaiyu lode gold deposit, North China Craton: a link between craton reactivation and gold veining. Econ. Geol. 107, 43–79.

Lin, S.Z., Zhu, G., Yan, L.J., Song, L.H., Liu, B., 2013a. Structural and chronological constraints on a Late Paleozoic shortening event in the Yanshan Tectonic Belt. Chin. Sci. Bull. 58, 3922–3936.

Lin, W., Faure, M., Chen, Y., Ji, W., Wang, F., Wu, L., Charles, N., Wang, J., Wang, Q., 2013b. Late Mesozoic compressional to extensional tectonics in the Yiwulüshan massif, NE China and its bearing on the evolution of the Yinshan–Yanshan orogenic belt: Part I: Structural analyses and geochronological constraints. Gondwana Res. 23, 54–77.

Liu, G., 1992. Regional Metallogenic Model Research on Chifeng–Chaoyang Gold Province. Northeast University of Technology Press, Shenyang (in Chinese).

Liu, W., Yang, J.H., Li, C.F., 2003. Thermochronology of three major faults in the Chifeng region, Inner Mongolia of China. Acta Petrol. Sin. 19, 717–728 (in Chinese with English abstract).

Liu, Y.S., Hu, Z.C., Gao, S., Güenther, D., Xu, J., Gao, C.G., Chen, H.H., 2008. In situ analysis of major and trace elements of anhydrous minerals by LA-ICP-MS without applying an internal standard. Chem. Geol. 257, 34–43.

Liu, Y.S., Gao, S., Hu, Z.C., Gao, C.G., Zong, K.Q., Wang, D.B., 2010. Continental and oceanic crust recycling-induced melt-peridotite interactions in the Trans-North China Orogen: U–Pb dating, Hf isotopes and trace elements in zircons from mantle xenoliths. J. Petrol. 51, 537–571.

Liu, S.W., Santosh, M., Wang, W., Bai, X., Yang, P.T., 2011. Zircon U–Pb chronology of the Jianping Complex: implications for the Precambrian crustal evolution history of the northern margin of North China Craton. Gondwana Res. 20, 48–63.

Liu, J.L., Shen, L., Ji, M., Guan, H.M., Zhang, Z.C., Zhao, Z.D., 2013. The Liaonan/Wanfu metamorphic core complexes in the Liaodong Peninsula: two stages of exhumation and constraints on the destruction of the North China Craton. Tectonics 32, 1121–1141.

Ludwig, K.R., 2003. User's manual for Isoplot 3.0 — a geochronological toolkit for Microsoft Excel. 4. Berkeley Geochronology Center, Special Publication, pp. 1–70.

Mao, J.W., Goldfarb, R.J., Zhang, Z.W., Xu, W.Y., Qiu, Y.M., Deng, J., 2002. Gold deposits in the Xiaoqinling–Xiong'ershan region, Qinling Mountains, central China. Miner. Deposita 37, 306–325.

Mao, J.W., Wang, Y.T., Li, H.M., Pirajno, F., Zhang, C.Q., Wang, R.T., 2008. The relationship of mantle-derived fluids to gold metallogenesis in the Jiaodong Peninsula: evidence from D–O–C–S isotope systematics. Ore Geol. Rev. 33, 361–381.

Maruyama, S., Isozaki, Y., Kimura, G., Terabayashi, M., 1997. Paleogeographic maps of the Japanese Islands: plate tectonic synthesis from 750 Ma to the present. Island Arc 6, 121–142.

Meng, Q.R., 2003. What drove late Mesozoic extension of the northern China–Mongolia tract? Tectonophysics 369, 155–174.

Miao, L.C., Fan, W.M., Qiu, Y.M., Mcnaughton, N.J., Groves, D.I., 2003. Zircon SHRIMP U–Pb geochronology of the granitoid intrusions from Jinchanggouliang–Erdaogou gold orefield and its significance. Acta Petrol. Sin. 19, 71–80 (in Chinese with English abstract).

Moritz, R., Ghazban, F., Singer, B.S., 2006. Eocene gold ore formation at Muteh, Sanandaj–Sirjan tectonic zone, western Iran: a result of late-stage extension and exhumation of metamorphic basement rocks within the Zagros orogen. Econ. Geol. 101, 1497–1524.

Ohmoto, H., 1972. Systematics of sulfur and carbon isotopes in hydrothermal ore deposits. Econ. Geol. 67, 551–578.

Ouyang, Z.X., 2010. Comparison of geochronology and origin of the late Mesozoic granitoids from major metamorphic core complexs in the North China craton and their significance(MSc. Degree Thesis) Chinese Academy of Geological Sciences, Beijing (in Chinese with English abstract).

Reiners, P.W., Ehlers, T.A., Zeitler, P.K., 2005. Past, present, and future of thermochronology. Rev. Mineral. Geochem. 58, 1–18.

Ren, J., Tamaki, K., Li, S.T., Zhang, J.X., 2002. Late Mesozoic and Cenozoic rifting and its dynamic setting in Eastern China and adjacent areas. Tectonophysics 344, 175–205.

Ridley, J.R., Diamond, L.W., 2000. Fluid chemistry of orogenic lode gold deposits and implications for genetic models. SEG Rev. 13, 141–162.

Rohrmeier, M.K., von Quadtp, A., Driesner, T., Heinrich, C.A., Handler, R., Ovtcharova, M., Ivanov, Z., Petrov, P., Sarov, S., Peytcheva, I., 2013. Post-orogenic extension and hydrothermal ore formation: high-precision geochronology of the Central Rhodopian metamorphic core complex (Bulgaria–Greece). Econ. Geol. 108, 691–718.

Schmidt, M.W., 1992. Amphibole composition in tonalite as a function of pressure: an experimental calibration of the Al-in-hornblende barometer. Contrib. Mineral. Petrol. 110, 304–310.

Shao, J.A., Zhang, L.Q., Jia, W., Wang, P.Y., 2001. Harkin metamorphic core complex in Inner Mongolia and its upwelling mechanism. Acta Petrol. Sin. 17, 190–283 (in Chinese with English abstract).

Sibson, R.H., 1994. Crustal stress, faulting and fluid flow. Geol. Soc. Lond., Spec. Publ. 78, 69–84.

Siebenaller, L., Boiron, M.C., Vanderhaeghe, O., Hibsch, C., Jessell, M.W., Andre-Mayer, A.S., France-Lanord, C., Photiades, A., 2013. Fluid record of rock exhumation across the brittle–ductile transition during formation of a Metamorphic Core Complex (Naxos Island, Cyclades, Greece). J. Metamorph. Geol. 31, 313–338.

Song, Y., Jiang, S.H., Bagas, L., Li, C., Hu, J., Wang, S., Zhou, W., Ding, H., 2016. The geology and geochemistry of Jinchangyu gold deposit, North China Craton: Implications for metallogenesis and geodynamic setting. Ore Geol. Rev. 73, 313–329.

Sun, W.D., Ding, X., Hu, Y.H., Li, X.H., 2007. The golden transformation of the Cretaceous plate subduction in the west Pacific. Earth Planet. Sci. Lett. 262, 533–542.

Sun, S.K., Liu, H.T., Chu, S.X., 2012. Origin of the Paishanlou monzogranite in Liaoning Province and its genetic connection with gold mineralization. Acta Petrol. Sin. 28, 607–618 (in Chinese with English abstract).

Tan, J., Wei, J., Li, Y., Tan, W., Guo, D., Yang, C., 2007. Geochemical characteristics of Late Mesozoic dikes, Jiaodong Peninsula, North China craton: petrogenesis and geodynamic setting. Int. Geol. Rev. 49, 931–946.

Tan, J., Wei, J., Audétat, A., Pettke, T., 2012. Source of metals in the Guocheng gold deposit, Jiaodong Peninsula, North China Craton: Link to early Cretaceous mafic magmatism originating from Paleoproterozoic metasomatized lithospheric mantle. Ore Geol. Rev. 48, 70–87.

Taylor, H.P., 1974. The application of oxygen and hydrogen isotope studies to problems of hydrothermal alteration and ore deposition. Econ. Geol. 69, 843–883.

Trumbull, R.B., Liu, H., Lehrberger, G., Satir, M., Wimbauer, T., Morteani, G., 1996. Granitoid-hosted gold deposits in the Anjiayingzi district of Inner Mongolia, People's Republic of China. Econ. Geol. 91, 875–895.

Wang, Y.W., 1993. Study on the stable isotopic geochemistry of gold deposits in western Liaoning. Contrib. Geol. Mineral Resour. Res. 8, 73–86 (in Chinese with English abstract).

Wang, X.S., Zheng, Y.D., 2005. ⁴⁰Ar/³⁹Ar age constraints on the ductile deformation of the detachment system of the Louzidian core complex, southern Chifeng, China. Geol. Rev. 51, 96–104 (in Chinese with English abstract).

Wang, S.Q., Sun, C.Z., Cui, W.Y., 1994. Geology of Gold Deposits from Chifeng, Inner Mongolia. Inner Mongolia People's Publishing House, Hohhot (in Chinese).

Wang, X.S., Zheng, Y.D., Jia, W., 2004. Extension of the Louzidian metamorphic core complex and development of supradetachment basins in southern Chifeng, Inner Mongolia, China. Acta Geol. Sin. 78, 237–245.

Wang, X.S., Zheng, Y.D., Liu, Y.L., Bradley, R., Scott, F., 2006. Timing of the chloritic zone from Louzidian detachment system, southern Chifeng, Inner Mongolia. Prog. Nat. Sci. 16, 902–906 (in Chinese).

Wang, T., Zheng, Y.D., Zhang, J.J., Zeng, L.S., Donskaya, T., Guo, L., Li, J.B., 2011. Pattern and kinematic polarity of late Mesozoic extension in continental NE Asia: perspectives from metamorphic core complexes. Tectonics 30, TC6007.

Wei, J.H., Liu, C.Q., Tang, H.F., 2002. Rb–Sr isotopic chronology of the Au-bearing quartz veins in gold deposits in the eastern part of North China platform. Chinese J. Geochem. 21, 374–382.

Whitney, D.L., Teyssier, C., Rey, P., Buck, W.R., 2013. Continental and oceanic core complexes. Geol. Soc. Am. Bull. 125, 273–298.

Wilkinson, J.J., 2001. Fluid inclusions in hydrothermal ore deposits. Lithos 55, 229–272.

Wu, F.Y., Lin, J.Q., Wilde, S.A., Zhang, X.O., Yang, J.H., 2005. Nature and significance of the Early Cretaceous giant igneous event in eastern China. Earth Planet. Sci. Lett. 233, 103–119.

Wu, F.Y., Zhang, Y.B., Yang, J.H., Xie, L.W., Yang, Y.H., 2008. Zircon U–Pb and Hf isotopic constraints on the Early Archean crustal evolution in Anshan of the North China Craton. Precambrian Res. 167, 339–362.

Xiao, W.J., Windley, B.F., Huang, B.C., Han, C.M., Yuan, C., Chen, H.L., Sun, M., Sun, S., Li, J.L., 2009. End-Permian to mid-Triassic termination of the accretionary processes of the southern Altaids: implications for the geodynamic evolution, Phanerozoic continental growth, and metallogeny of Central Asia. Int. J. Earth Sci. 98, 1189–1217.

Yang, J.H., Wu, F.Y., Wilde, S.A., 2003. A review of the geodynamic setting of large-scale Late Mesozoic gold mineralization in the North China Craton: an association with lithospheric thinning. Ore Geol. Rev. 23, 125–152.

Yang, J.H., Wu, F.Y., Chung, S.L., Lo, C.H., Wilde, S.A., Davis, G.A., 2007. Rapid exhumation and cooling of the Liaonan metamorphic core complex: Inferences from ⁴⁰Ar/³⁹Ar thermochronology and implications for Late Mesozoic extension in the eastern North China Craton. Geol. Soc. Am. Bull. 119, 1405–1414.

Yang, J.H., Wu, F.Y., Wilde, S.A., Chen, F.K., Liu, X.M., Xie, L.W., 2008. Petrogenesis of an alkali syenite–granite–rhyolite suite in the Yanshan fold and thrust belt, eastern North China Craton: geochronological, geochemical and Nd–Sr–Hf isotopic evidence for lithospheric thinning. J. Petrol. 49, 315–351.

Yang, L.Q., Deng, J., Goldfarb, R.J., Zhang, J., Gao, B.F., Wang, Z.L., 2014. ⁴⁰Ar/³⁹Ar geochronological constraints on the formation of the Dayingezhuang gold deposit: New implications for timing and duration of hydrothermal activity in the Jiaodong gold province, China. Gondwana Res. 25, 1469–1483.

Yao, L.J., Yan, D.P., Hu, L., 2007. Structure style and temperature–pressure estimation of the detachment fault zone around Fangshan dome, Western Hills of Beijing. Earth Sci. 32, 357–365 (in Chinese with English abstract).

Zhai, M., Santosh, M., 2011. The early Precambrian odyssey of the North China Craton: a synoptic overview. Gondwana Res. 20, 6–25.

Zhai, M., Santosh, M., 2013. Metallogeny of the North China Craton: link with secular changes in the evolving Earth. Gondwana Res. 24, 275–297.

Zhang, S.H., Zhao, Y., 2013. Mid-crustal emplacement and deformation of plutons in an Andean-style continental arc along the northern margin of the North China Block and tectonic implications. Tectonophysics 608, 176–195.

Zhang, X.H., Li, T.S., Pu, Z.P., Wang, H., 2002. ⁴⁰Ar–³⁹Ar ages of the Louzidian–Dachengzi ductile shear zone near Chifeng, Inner Mongolia and their tectonic significance. Chin. Sci. Bull. 47, 1292–1297.

Zhang, X.H., Liu, Q., Ma, Y.J., Wang, H., 2005. Geology, fluid inclusions, isotope geochemistry, and geochronology of the Paishanlou shear zone-hosted gold deposit, North China Craton. Ore Geol. Rev. 26, 325–348.

Zhang, S.H., Zhao, Y., Song, B., Hu, J.M., Liu, S.W., Yang, Y.H., Chen, F.K., Liu, X.M., Liu, J., 2009. Contrasting Late Carboniferous and Late Permian–Middle Triassic intrusive suites from the northern margin of the North China craton: geochronology, petrogenesis, and tectonic implications. Geol. Soc. Am. Bull. 121, 181–200.

Zhao, G.C., Zhai, M.G., 2013. Lithotectonic elements of Precambrian basement in the North China Craton: review and tectonic implications. Gondwana Res. 23, 1207–1240.

L. Fu et al. / Ore Geology Reviews 73 (2016) 222–240

Zhao, G.H., Wilde, S.A., Cawood, P.A., Sun, M., 2001. Archean blocks and their boundaries in the North China Craton: lithological, geochemical, structural and P–T path constraints and tectonic evolution. Precambrian Res. 107, 45–73.

Zhao, H.X., Jiang, S.Y., Frimmel, H.E., Dai, B.Z., Ma, L., 2012. Geochemistry, geochronology and Sr–Nd–Hf isotopes of two Mesozoic granitoids in the Xiaoqinling gold district: implication for large-scale lithospheric thinning in the North China Craton. Chem. Geol. 294–295, 173–189.

Zheng, X.Z., Zhang, K.W., Guan, H., Li, X.Y., Li, D.Z., 1995. Isotope geochemistry of the eastern Kalaqin gold deposit. Gold Sci. Tech. 3, 26–32 (in Chinese).

Zheng, Y.F., Zhang, L.F., McClelland, W.C., Cuthbert, S., 2012. Processes in continental collision zones: preface. Lithos 136–139, 1–9.

Zhou, T.H., Goldfarb, R.J., 2002. Tectonics and metallogeny of gold deposits in China. Miner. Deposita 37, 247–248.

Zhou, Z.J., Chen, Y.J., Jiang, S.Y., Zhao, H.X., Qin, Y., Hu, C.J., 2014. Geology, geochemistry and ore genesis of the Wenyu gold deposit, Xiaoqinling gold field, Qinling Orogen, southern margin of North China Craton. Ore Geol. Rev. 59, 1–20.

Zhu, G., Jiang, D.Z., Zhang, B.L., Chen, Y., 2012. Destruction of the eastern North China Craton in a backarc setting: evidence from crustal deformation kinematics. Gondwana Res. 22, 86–103.